

PATTERN FORMATION AND BISTABILITY IN FLOW BETWEEN COUNTERROTATING CYLINDERS

M. GOLUBITSKY

Department of Mathematics, University of Houston, Houston, TX 77004, USA

and

W.F. LANGFORD

Department of Mathematics and Statistics, University of Guelph, Guelph, Ontario, Canada N1G 2W1

Received 16 February 1988

Revised manuscript received 24 May 1988

Communicated by J. Guckenheimer

In the Taylor–Couette experiment on fluid flow between counterrotating cylinders, there is a bicritical point where the onset of instabilities to Taylor vortex flow (a steady-state bifurcation) and spiral vortex flow (a Hopf bifurcation) meet. The nonlinear mode interactions near this bicritical point are analyzed, exploiting the role of symmetry in the bifurcation theory, and with emphasis on the relevance to experiments, for a range of radius ratios $0.43 \leq \eta \leq 0.98$. The mechanism of the pattern formation is elucidated, and several new flow patterns and transitions are predicted, including wavy vortices, bistability, hysteresis, and up to 7 quasiperiodic flows.

Introduction

Since the seminal work of Taylor [1], investigators have sought to explain the intriguing variety of patterns observed in the Taylor–Couette experiment, that is, in the flow of a fluid contained between two concentric and independently rotating cylinders. (A comprehensive survey and bibliography of both theoretical and experimental work is given by DiPrima and Swinney [2]). The recent experimental study of Andereck et al. [3] provides a detailed map of the flow patterns (or states) observed as the rotation speeds of the two cylinders are varied quasistatically for a fixed radius ratio $\eta = 0.883$, see fig. 1. If the two cylinders are rotated in the same direction, then the more complex flow patterns are observed only for large values of the Reynolds numbers; however, in the case of counterrotating cylinders, complex flow patterns may appear in close proximity to the primary transition from laminar Couette flow, at relatively low Reynolds numbers. Recent advances in equivariant bifurcation theory (Golubitsky and Stewart [4]) make possible an explanation of these low Reynolds number complex flow patterns. This paper presents detailed calculations of Hopf and steady-state bifurcation mode interactions in the presence of symmetry, which are in agreement with experimental observation. The analysis covers a wide range of radius ratios η , from 0.43 to 0.98, and predicts new flow states, bistability and hysteresis behavior not previously reported. These predictions seem to be confirmed by experiments now in progress (Tagg et al. [5]). The results affirm the significance of equivariant bifurcation mode interactions for pattern formation in fluid dynamics, and may provide a paradigm for studies of pattern formation in other fields.

Following this Introduction, section 1 outlines the mathematical analysis involved in the reduction of the Navier–Stokes equations to a 6-dimensional mapping by the classical Liapunov–Schmidt procedure. Section 2 summarizes the consequences of the symmetry assumptions and gives the resulting normal form, following Golubitsky and Stewart [4] but with a new choice of coordinates which is more convenient for calculations. Section 3 describes the numerical computations. Finally, section 4 presents the detailed results and the conclusion of this investigation.

The remainder of this Introduction is divided into 3 parts. Part A describes the relevant experimental observations and the symmetries of the experiments, part B outlines the main results of this investigation, and part C reviews previous work as it relates to this paper.

A. Experiments and symmetries

Fig. 1 shows the flow regimes found by Andereck et al. [3], for experiments with counterrotating cylinders, and radius ratio $\eta = 0.883$. The coordinates R_1 and R_2 are the two Reynolds numbers, proportional to the rotation speeds of the inner and outer cylinders respectively, and opposite in sign because the cylinders are counterrotating (precise definitions are given in section 1). The flow patterns which are of interest in this paper are:

AZI = azimuthal laminar flow (also called Couette flow COU),
 TVF = Taylor vortex flow,
 SPI = spiral vortices,
 IPS = interpenetrating spirals,
 WVF = wavy vortex flow,
 MWV = modulated wavy vortices,
 RIB = ribbons (nonaxisymmetric simple mode),
 TWI = twisted vortices,
 MSP = modulated spirals,
 MTW = modulated twisted vortices.

See Andereck et al. [3] for identification of the outer flow regimes in fig. 1. This paper is concerned with the neighborhood where the regimes AZI, TVF, SPI and IPS appear to meet in fig. 1.

Fig. 2 presents photographs of the flow patterns for the cases TVF, WVF and SPI. The flow patterns are visualized by adding small platelike particles (called kalliroscope) to the fluid, which align themselves in the direction of the flow and reflect light. For sufficiently small R_1 (below the lowest curve in fig. 1), the observed flow is primarily an azimuthal laminar flow here called AZI or Couette flow, which is constant in time and spatially constant in the axial and azimuthal directions. (Superimposed on the laminar Couette flow one observes weak Ekman cells due to end effects and finite cylinder length. The effects of finite length on the AZI and TVF flow patterns are partially explained in terms of the Ginzburg–Landau amplitude equation, see Ahlers et al. [6] and further references therein. Finite length effects are excluded from our calculations, an assumption discussed further below.) The three flow patterns in fig. 2 may be obtained by the following experimental procedure. A rotation speed for the outer cylinder is chosen (this determines R_2), and the outer cylinder is slowly accelerated to and then held at this constant speed. Next the inner cylinder is slowly accelerated to the speed determined by R_1 . If R_2 is negative but near 0, or positive with any magnitude, then as R_1 increases the first transition from AZI is to TVF, which is shown in fig. 2(a). On further increase of R_1 at the same R_2 , one next observes a transition from TVF to WVF,

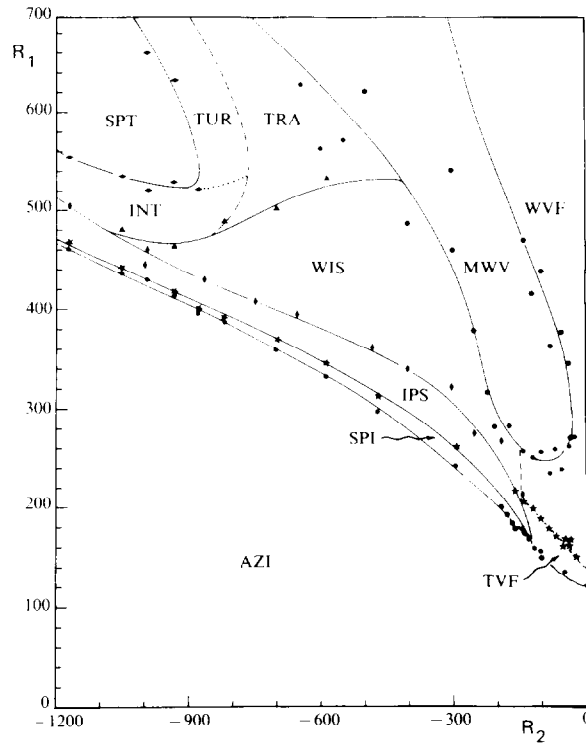


Fig. 1. The flow-regime diagram for counterrotating cylinders and $\eta = 0.883$, from experiments of Andereck et al. [3]. The abbreviations AZI, etc. used for the different flow patterns are explained in the text.

see fig. 2(B). However, for more negative values of R_2 (stronger counterrotation) as R_1 is increased the first transition from AZI is to SPI, see fig. 2(c). All of these transitions are shown as boundary curves in fig. 1. Andereck et al. [3] only briefly describe the bicritical region, where the TVF and SPI transitions meet: “Near $R_2 = -155, \dots$ increasing R_1 leads to a complicated series of transitions from Taylor vortex flow to spirals and mixtures of the two flows. The order of these transitions is not well established...”.

Though extensive in Reynolds numbers, the study of Andereck et al. [3] is limited to a single value of the radius ratio $\eta = 0.883$. Snyder [7] experimentally determined the primary transition boundary for 4 radius ratios, $\eta = 0.20, 0.50, 0.80$ and 0.959 , and found the bicritical points (where the TVF and SPI transitions meet) to be strongly dependent on η . His measurements confirmed the linear stability analysis of Krueger et al. [8]. These and other experiments, however, leave open the selection of flow patterns beyond the primary transition boundary near bicriticality. New experiments are now underway (Tagg et al. [5]) to clarify these transitions near the bicritical point.

The symmetries of the experimental apparatus and of the flow patterns play a fundamental role in the analysis of this paper. First we observe that, since the underlying physical laws (the Navier–Stokes equations) are invariant under the Euclidean group E_3 of all translations, rotations, and reflections of space, the group of symmetries of the experiment is a subgroup of E_3 determined by the shape of the domain and the boundary conditions. The most obvious symmetry of the Taylor–Couette system is that obtained by rotation of the whole apparatus about the common axis of the two cylinders. These rotations lead to an $SO(2)$ azimuthal symmetry. There is also an approximate axial symmetry evident in the photographs in fig. 2. In fact, many of the observed flow patterns appear to be periodic in the axial

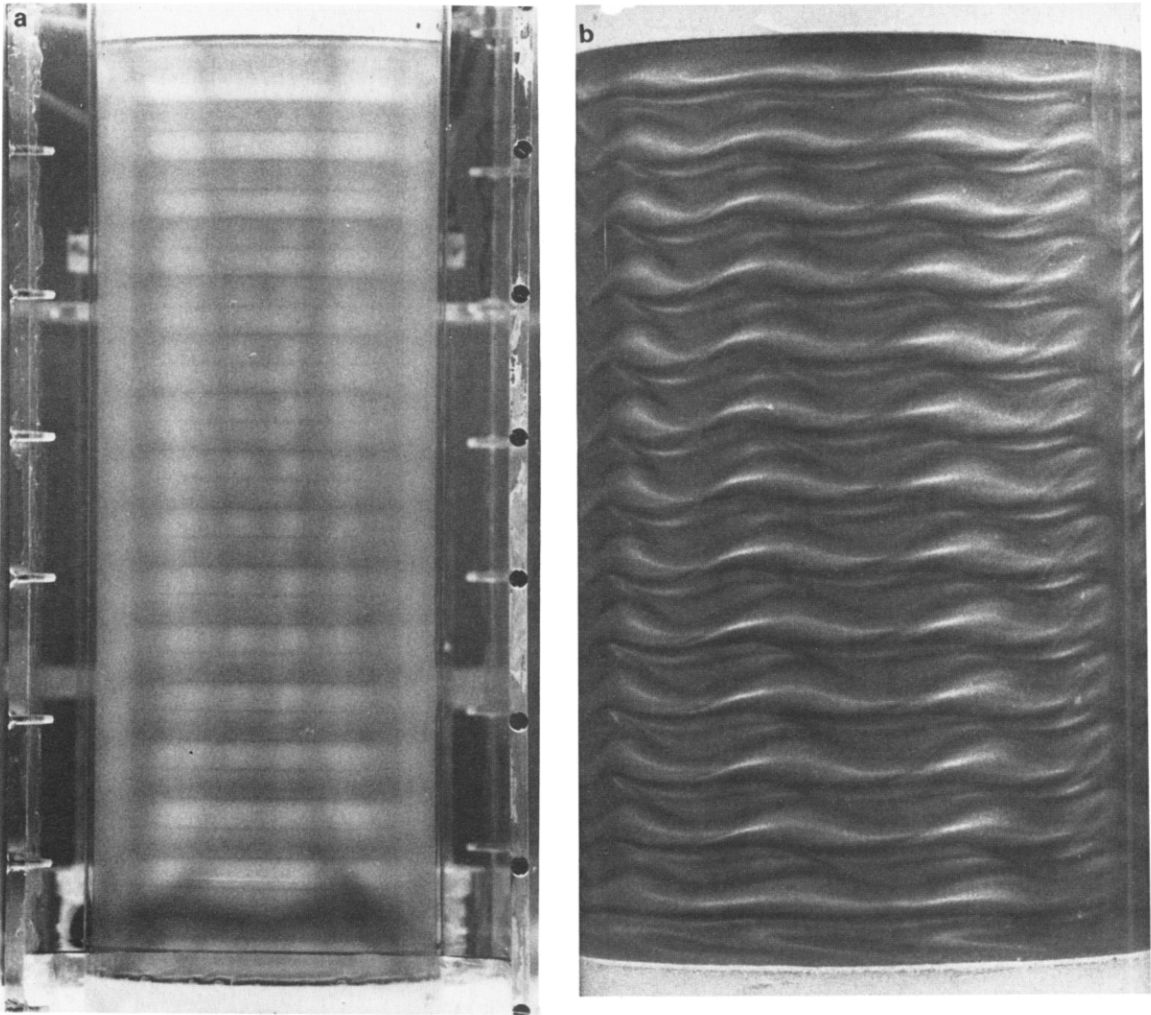


Fig. 2. Photographs of experimentally observed flow patterns; (a) Taylor vortex flow (TVF), (b) wavy vortex flow (WVF), (c) spiral vortices (SPI). Courtesy of R. Tagg and H.L. Swinney.

direction, within the central portion of long cylinders. (For short cylinders, it is well known that this is not the case, for example Benjamin [9] emphasized the importance of finite length effects.) Throughout this paper we assume that the fluid flow pattern is periodic in the axial direction, an assumption which goes back at least to Taylor [1], and is adopted in the majority of papers cited here. This assumption is often called the infinite cylinder approximation, because theoretically an axially periodic flow pattern can be extended indefinitely in the axial direction. However, we prefer the mathematically equivalent interpretation of a finite cylinder, one period in length, with the two ends identified, i.e. with periodic boundary conditions. Thus axial translations are identified with the action of a circle group. This assumption will be justified if the results agree with experimental measurements taken in the central portion of sufficiently long cylinders. In addition to this axial periodicity, we observe that the cylinders are symmetric with respect to reflection through a plane perpendicular to the axis. Then the full axial symmetries may be

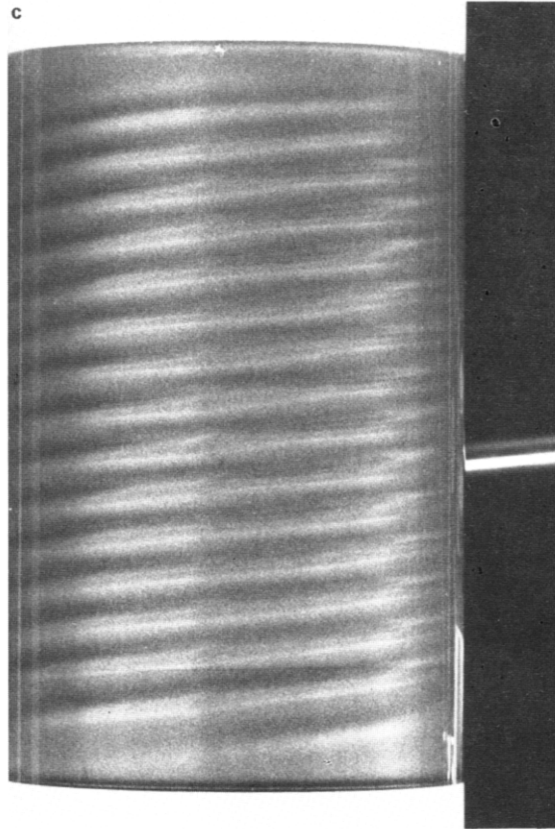


Fig. 2. Continued.

identified with the group $O(2)$, the orthogonal group of rotations and reflections of the plane. Since the axial $O(2)$ and the azimuthal $SO(2)$ symmetries commute, the total spatial symmetries of the model form the group $\Gamma = O(2) \times SO(2)$. The consequences of these symmetry assumptions are presented in section 2.

Inspection of the flow patterns observed in the experiments reveals that they have symmetries which can be identified with subgroups of Γ . For example, Couette flow (neglecting end effects) is invariant under the full symmetry group Γ . Flow patterns with more structure correspond to smaller subgroups. In fig. 2, Taylor vortices (TVF) have the symmetry $Z_2 \times SO(2)$ of axial flips and azimuthal rotations, spirals (SPI) have the symmetry $\widetilde{SO}(2)$ of a simultaneous axial translation and azimuthal rotation, and wavy vortices (WVF) have the symmetry $Z_2(\kappa \cdot (\pi, \pi))$ of a simultaneous axial flip and azimuthal half-period rotation. (See section 2 for an explanation of the group-theoretic notation used here.) In this way, experimentally observed flow patterns may be identified conveniently by their symmetry subgroups.

Furthermore, the experimental observation that these flow patterns break the original symmetry of the apparatus leads to predictions about the multiplicity of the eigenvalues found in the analysis to be described in section 1. For example, it is known (since Taylor [1]) that the bifurcation of Taylor vortices corresponds to the existence of a zero eigenvalue for the linearization of the boundary value problem about Couette flow. The Taylor vortices are not invariant under the axial translational symmetry of the

apparatus. From a given set of Taylor vortices, we can obtain a continuum of congruent Taylor vortices, by axial translation through any portion of one period. These are distinct and independent, but all are solutions of the boundary value problem, in view of our assumption of axial $O(2)$ symmetry. Therefore the zero eigenvalue must have at least a 2-dimensional eigenspace. Genericity leads to the conclusion that it is exactly of multiplicity 2. Similarly, the bifurcation of spiral vortices corresponds to the existence of pure imaginary eigenvalues $\pm i\omega$ (a Hopf bifurcation). But upward spiraling vortices are clearly distinct from downward spiraling vortices. The fact that spirals break the reflectional as well as translational $O(2)$ axial symmetry implies that these imaginary eigenvalues are generically double. These predictions are confirmed by the calculations, see section 1. For a more complete discussion of these group-theoretic ideas, see Golubitsky et al. [10].

B. Outline of results

The results of this paper, presented in detail in sections 1–4, are briefly outlined here.

The Navier–Stokes partial differential equations for the Taylor–Couette experiment have been reduced by the Liapunov–Schmidt procedure to a 6-dimensional bifurcation equation or normal form, in a neighborhood of the bicritical point for the Hopf/steady-state mode interaction. This reduction preserves branches of stationary and periodic solutions, together with their stabilities, and gives some information about more complicated dynamics such as tori.

The symmetry group $\Gamma = O(2) \times SO(2)$ restricts the 6-dimensional bifurcation equation to a very special normal form. The possible branches of solutions of the normal form equations have been classified, along with their stabilities, so far as these are determined locally by cubic terms in the normal form. These solutions include the following, with the same symmetries as the observed flows: AZI, TVF, WVF and SPI described above, and also twisted vortices (TWI), and 2-frequency modulated wavy vortices (MWV); as well as ribbons (RIB), the last not observed by Andereck et al. [3]. In addition several new types of flow states are found: a second 2-frequency MWV, 3-frequency MWV, analogous 2- and 3-frequency modulated twisted vortices (MTW), and a new type of 2-frequency modulated spiral flow (MSP); in total there are 7 possible quasiperiodic flows.

The coefficients of the normal form equations, calculated on a microcomputer, determine the bifurcation diagrams, presented here for a range of radius ratios from $\eta = 0.43$ to $\eta = 0.98$. The numerical results give explicit predictions which can be compared directly with experimental data. In experiments one may only expect to observe flow patterns corresponding to solutions which are stable (asymptotically stable in the sense of Liapunov). The calculations show that most of the solutions in the previous paragraph are unstable and hence not observable. The only solutions found to be stable are AZI, TVF, WVF and SPI. The existence of stable AZI, TVF and SPI is in agreement with published experimental observations, however the observation of WVF near criticality has not been reported. Furthermore, the calculations predict the existence of parameter values at which SPI and either TVF or WVF exist and are stable simultaneously (bistability), and of jumps between the two states as the parameters change (hysteresis). Experiments now in progress (Tagg et al. [5]) appear to confirm all three new predictions. In fact the ambiguous observations of Andereck et al. [3] quoted in part A may be due in part to this bistability.

The analysis also explored the effects of radius ratio on pattern formation, near bicriticality. Over a range of wider gaps, $\eta = 0.43$ to $\eta = 0.80$, variation of the radius ratio was found to have negligible qualitative effect on the bifurcation diagrams. However, for narrow gaps, $\eta > 0.85$, the effect is dramatic. One encounters several additional degeneracies in cubic coefficients which change stabilities of TVF, MVF

and SPI, as well as the proximity of additional bicritical points corresponding to Hopf/Hopf mode interactions. The latter gives a plausible explanation for the discrepancy between the observation of IPS by Andereck et al. [3], and the absence of IPS in the results of this paper, since the IPS mode arises naturally in Hopf/Hopf mode interactions, see Chossat et al. [11]. Because of these degeneracies, the results of this paper are most applicable for wider gaps ($\eta \leq 0.85$); narrower gaps require further effort.

Of the possible quasiperiodic flows, stability has been computed only for the modulated spiral solution, and it is always unstable. Further investigation of the quasiperiodic flows is left for a future paper.

The results of the calculations have been compared with available experimental data, from measurements in the central portion of moderately long cylinders (aspect ratios about 30). The quantitative agreement of these results with experimental data validates the assumption of axial periodicity, and supports the hypothesis that end effects are not important in this context.

The analysis presented in this paper is relevant to the understanding of the transition to turbulence in the Taylor–Couette experiment. It lays the foundation for investigation of the mode-interaction route to turbulence, as explained below.

Finally, on the fundamental question of the origin of the flow patterns observed in the experiments, this analysis implies that both the form and the variety of the patterns are due principally to the symmetry in the geometry of the apparatus and to generic implications of equivalent bifurcation theory, and not to the physics of the fluid as expressed by the Navier–Stokes equations. This conclusion suggests that similar analyses will be fruitful in explaining pattern formation in other fields, when symmetry is present.

C. Previous work

Hopf and steady-state mode interactions have been studied by Langford [12], Holmes [13], Iooss and Langford [14], Guckenheimer [15] and others; see Guckenheimer and Holmes [16] and further references therein. In one-parameter families of differential equations, Hopf bifurcation and steady-state bifurcation each occur generically (modulo constraints or symmetries). The coalescence of these two bifurcations can be expected to occur in 2-parameter families, and normal form analysis shows that nonlinear interactions near the coalescence lead to secondary bifurcations of time-periodic solutions and even to quasiperiodic solutions (2-tori). The analogy between the sequence of bifurcations occurring in Hopf/steady-state mode interactions and the “main sequence” of transitions observed in the Taylor–Couette experiment was pointed out by Langford [12]. Coalescence of Hopf and steady-state bifurcations in the Taylor–Couette problem is not unexpected, since there are 3 independent parameters available (the 2 cylinder rotation speeds and the radius ratio). Linear stability analysis of Krueger et al. [8] (extended by Langford et al. [17]) demonstrated the existence of such bicritical points, see section 1. However, the analysis of mode interactions under generic assumptions does not apply here, because of the special symmetries of the Taylor–Couette apparatus, which require an equivariant version of the bifurcation theory. The general analysis of Hopf/steady-state mode interactions in the presence of the $O(2) \times SO(2)$ symmetry of the Taylor–Couette apparatus was first carried out by Golubitsky and Stewart [4], in a coordinate system less convenient for calculations than the one presented here. See Golubitsky et al. [10] for a more detailed exposition of the present approach.

The landmark paper of Davey et al. [18] explained the instability of Taylor vortices to nonaxisymmetric disturbances as a nonlinear interaction between the first two unstable modes from Couette flow; i.e. as a Hopf/steady-state mode interaction in the language of this paper. Their analysis used amplitude expansions in a 6-dimensional system, as here, and they found the 5 solution types are called Taylor vortices,

wavy vortices, twisted vortices, spirals and ribbons (but they called ribbons “the nonaxisymmetric simple mode”). Without explicitly exploiting the symmetries, they calculated the cubic coefficients; this was extended to fifth order by Eagles [19]. They were not able to justify mathematically their reduction to 6 (or fewer) modes, since they considered only the case of a fixed outer cylinder where the bicriticality (coalescence) does not actually occur. They worked in the small gap limit, in order to carry out the asymptotic analysis. In the case of counterrotation of the two cylinders, bicriticality is known to occur over a wide range of radius ratios (Langford et al. [17]). Thus the present paper is able to extend the asymptotic results of Davey et al. [18] globally in the radius ratio, to perform the reduction to 6 dimensions (or less) with greater mathematical rigor, to reveal new flow states, and to explain the mechanism underlying the observed pattern formation.

DiPrima and Grannick [20] extended the earlier linear stability analysis of Krueger et al. [8] in the case of counterrotating cylinders, into the nonlinear regime, using the amplitude expansion technique of Davey et al. [18], for a fixed radius ratio $\eta = 0.95$. They calculated the direction and stability of the primary bifurcation solution on both sides of the bicritical point. To the left side, they found that the primary bifurcation always yields simultaneously spirals and ribbons (the nonaxisymmetric simple mode); the ribbons are never stable, and the spirals vary between stable supercritical and unstable subcritical. The azimuthal mode number m increases with the counterrotation. To the right side, where Taylor vortices bifurcate first, they discovered a small interval of subcritical instability of Taylor vortices near the bicritical point.

The stability of Taylor vortices to nonaxisymmetric disturbances for counterrotating cylinders was studied by Jones [21], using a Chebyshev collocation procedure. He computed the bicritical curve (between Taylor vortices and spirals), and the curve of transition to subcriticality of Taylor vortices, for $0.5 < \eta < 1.0$.

The simultaneous bifurcation of spirals and ribbons was explained by Chossat and Iooss [22], as a Hopf bifurcation in the presence of the axial $O(2)$ symmetry (periodicity and reflection) of the flow. Demay and Iooss [23] calculated the cubic coefficients which determine relative stability of spirals and ribbons, for $\eta = 0.95$ and $\eta = 0.75$, and for a variety of azimuthal mode numbers, and predicted the existence of stable ribbons for $\eta = 0.75$. Chossat et al. [11] have calculated the cubic coefficients for the case of the Hopf/Hopf mode interaction, which occurs for stronger counterrotation than that considered here. These calculations are based on normal form techniques theoretically equivalent to the technique used here, see Chossat and Golubitsky [24]. Recently, the normal form for Taylor vortices has been calculated to fifth order using Macsyma computer algebra by Laure and Demay [25], and the singularity of codimension 3, with vanishing cubic Taylor vortex coefficient in the 6-dimensional normal form, has been considered by Signoret and Iooss [26]. Laure [27] presented the normal form to seventh order, for the codimension-3 singularity corresponding to transition between stable spirals stable ribbons, and found an unstable quasiperiodic flow and hysteresis between spirals and ribbons.

Independently, DiPrima et al. [28] have studied Hopf/steady-state mode interactions for flow between counterrotating cylinders, using a center manifold approach, and reported on preliminary findings which are consistent with those presented here. In particular, they noted the possibility of solutions other than those reported by Davey et al. [18], and pointed out the importance of fifth order terms where the cubic Taylor vortex coefficient changes sign.

One of the major problems of fluid dynamics today is that of understanding the transition to turbulence. There is mounting evidence that, at least in some systems having small spacial scales and/or symmetries, low dimensional “strange attractors” play an essential role, see Lanford [29] and Guckenheimer [30]. (Here “strange attractor” means a bounded invariant set in the phase space, with local exponential divergence of trajectories, and contained in the interior of an open region in which all trajectories converge to the

attractor as $t \rightarrow \infty$.) The Taylor–Couette experimental is one of the most thoroughly studied in this regard. Brandstätter et al. [31] calculated Liapunov exponents, phase portraits and power spectra from experimental measurements taken just above the onset of turbulence, and found convincing evidence of a strange attractor. The possible existence of such a strange attractor is of great significance, because it allows a reduction of the dynamical system from the infinite-dimensional phase space of the Navier–Stokes equations of fluid dynamics to the low finite dimensionality of the attractor itself, and thus, in principle, greatly simplifies the study of the dynamics. However, practical difficulties remain, because the reduction can never be carried out exactly, and even if it could, strange attractors involve global dynamics which can not be expressed by an explicit formula. Thus, for example it is very difficult to “find” a Lorenz attractor or a Roessler attractor explicitly in the Navier–Stokes equations. This difficulty is overcome in the mode-interaction route to turbulence. As indicated by the numerical studies of Langford [32, 33], the truncated normal form equations from Hopf/steady-state mode interactions can lead in a stable manner to chaotic dynamics, beyond the regime of periodic and quasiperiodic dynamics described above. This type of strange attractor is local, and is accessible via a reduction from the full Navier–Stokes equations; that is to say, only finitely many normal form coefficients are required, and they can be computed explicitly as in this paper. Thus this paper lays a foundation for further work, now under way, which investigates the possibilities of chaotic and quasiperiodic dynamics beyond the periodic regime, for mode interactions in the presence of the $O(2) \times SO(2)$ symmetries of the Taylor–Couette experiment.

1. Reduction of the Navier–Stokes equations to the 6-dimensional kernel

The analysis begins with the Navier–Stokes equations

$$\begin{aligned} \mathbf{u}_t &= \nu \nabla^2 \mathbf{u} - (\mathbf{u} \cdot \nabla) \mathbf{u} - \frac{1}{\rho} \nabla p, \\ \nabla \cdot \mathbf{u} &= 0, \end{aligned} \tag{1.1}$$

where

$$\begin{aligned} \mathbf{u}(t, \mathbf{x}) &= \text{velocity vector at time } t \text{ and } \mathbf{x} \equiv \mathbb{R}^3, \\ p &= \text{pressure}, \\ \rho &= \text{mass density}, \\ \nu &= \text{kinematic viscosity}. \end{aligned} \tag{1.2}$$

Let us introduce the additional notation

$$\begin{aligned} r_1 &= \text{inner cylinder radius}, \\ r_2 &= \text{outer cylinder radius}, \\ d &= \text{gap width} = r_2 - r_1, \\ \eta &= \text{radius ratio} = r_1/r_2, \\ \Omega_1 &= \text{inner cylinder angular velocity}, \end{aligned} \tag{1.3}$$

$\Omega_2 =$ outer cylinder angular velocity,
 $\mu = \Omega_1/\Omega_2$,
 $R_1 = r_1\Omega_1 d/\nu =$ inner cylinder Reynolds number,
 $R_2 = r_2\Omega_2 d/\nu =$ outer cylinder Reynolds number.

In the present work, $R_1 > 0$ and $R_2 < 0$. It is convenient to bring (1.1) into nondimensional form by rescaling lengths by d , velocities by the inner cylinder velocity $r_1\Omega_1$, and time t by the viscous time scale d^2/ν . Furthermore, given the cylindrical symmetry of the apparatus, it is natural to express (1.1) in cylindrical coordinates (r, θ, z) . We let u, v, w denote the corresponding components of \mathbf{u} in cylindrical coordinates. Then (1.1) in the new variables, with partial derivatives denoted by subscripts, is

$$\begin{aligned} u_t &= \nabla^2 u - \frac{2}{r^2} v_\theta - \frac{u}{r^2} - p_r - R_1 \left[uu_r + \frac{v}{r} u_\theta + wu_z - \frac{v^2}{r} \right], \\ v_t &= \nabla^2 v + \frac{2}{r^2} u_\theta - \frac{v}{r^2} - \frac{1}{r} p_\theta - R_1 \left[uv_r + \frac{v}{r} v_\theta + wv_z + \frac{uv}{r} \right], \\ w_t &= \nabla^2 w - p_z - R_1 \left[uw_r + \frac{v}{r} w_\theta + ww_z \right], \\ \nabla \cdot \mathbf{u} &= u_r + \frac{1}{r} u + \frac{1}{r} v_\theta + w_z = 0. \end{aligned} \tag{1.4}$$

The ‘no slip’ boundary conditions at the cylinder walls take the form

$$\begin{aligned} (u, v, w) &= (0, 1, 0) & \text{at } r = \eta/(1 - \eta), \\ (u, v, w) &= (0, \mu/\eta, 0) & \text{at } r = 1/(1 - \eta). \end{aligned} \tag{1.5}$$

As described in the Introduction, we assume that the flow \mathbf{u} is periodic in the z direction, with period $2\pi/k$, where k is the axial wave number to be determined numerically as explained below. We solve (1.4) over one period in z , with periodic end conditions, as well as azimuthal periodicity

$$\begin{aligned} \mathbf{u}(r, \theta, z) &= \mathbf{u}(r, \theta, z + 2\pi/k), \\ \mathbf{u}(r, \theta, z) &= \mathbf{u}(r, \theta + 2\pi, z). \end{aligned} \tag{1.6}$$

It is well known that the problem (1.4)–(1.6) has an exact time-independent solution, known as the Couette flow, given by

$$\begin{aligned} \mathbf{u}_c &= (0, v_c(r), 0), \quad p = p_c(r), \quad v_c(r) = A_c r + B_c/r, \\ A_c &= -\frac{\eta^2 - \mu}{\eta(1 + \eta)}, \quad B_c = \frac{\eta(1 - \mu)}{(1 - \eta)(1 - \eta^2)}, \quad p_c(r) = R_1 \int \frac{v_c(r)^2}{r} dr. \end{aligned} \tag{1.7}$$

Since Couette flow is independent of z and θ , it has the symmetry of the full group $\Gamma = \text{O}(2) \times \text{SO}(2)$ described in the Introduction. We are interested in the bifurcation from Couette flow to solutions with greater spatial structure, i.e. which break symmetry. To this end, we translate Couette flow to the trivial

solution, by substituting

$$\mathbf{u} = \mathbf{u}_c + \hat{\mathbf{u}}, \quad p = p_c + \hat{p}, \quad (1.8)$$

and then dropping the ‘‘hats’’. The resulting system is

$$\begin{aligned} u_t &= \nabla^2 u - \frac{u}{r^2} - \frac{2}{r^2} v_\theta - p_r - C(r) u_\theta + 2C(r) v - R_1 \left[uu_r + \frac{v}{r} u_\theta + w u_z - \frac{v^2}{r} \right], \\ v_t &= \nabla^2 v - \frac{v}{r^2} + \frac{2}{r^2} u_\theta - \frac{1}{r} p_\theta - C(r) v_\theta + 2Du - R_1 \left[uv_r + \frac{v}{r} v_\theta + w v_z + \frac{uv}{r} \right], \\ w_t &= \nabla^2 w - p_z - C(r) w_\theta - R_1 \left[uw_r + \frac{v}{r} w_\theta + w w_z \right], \\ u_r + \frac{1}{r} u + \frac{1}{r} v_\theta + w_z &= 0. \end{aligned} \quad (1.9)$$

The coefficients $C(r)$ and D appearing in (1.9) are defined by

$$\begin{aligned} D &= -R_1 A_c = \frac{\eta R_1 - R_2}{1 + \eta} > 0, \\ C(r) &= R_1 (A_c + B_c / r^2) = -D + \frac{\eta (R_1 - \eta R_2)}{(1 - \eta)(1 - \eta^2) r^2}. \end{aligned} \quad (1.10)$$

The boundary conditions for (1.9) state that the velocity is zero on the cylinder walls, and the periodicity conditions (1.6) are satisfied.

The analysis of bifurcation from Couette flow begins with a linear stability analysis of the trivial solution of (1.9). (The validity of the principle of linearized stability for the Navier–Stokes equations has been examined by several authors, see Sattinger [34] and references therein.) The linearization of (1.9) is obtained by dropping the bilinear terms (in square brackets). Then the stability of the trivial solution is determined by the eigenvalues λ of the eigenvalue problem

$$\begin{aligned} \lambda u &= \nabla^2 u - \frac{u}{r^2} - \frac{2}{r^2} v_\theta - p_r - C(r) u_\theta + 2C(r) v, \\ \lambda v &= \nabla^2 v - \frac{v}{r^2} + \frac{2}{r^2} u_\theta - \frac{1}{r} p_\theta - C(r) v_\theta + 2Du, \\ \lambda w &= \nabla^2 w - p_z - C(r) w_\theta, \\ \nabla \cdot \mathbf{u} &= 0. \end{aligned} \quad (1.11)$$

This eigenvalue problem has been studied by many authors. The axisymmetric case was investigated by Taylor [1] and Chandrasekhar [35]. The nonaxisymmetric case was studied by Krueger et al. [8], Demay and Iooss [23], and Langford et al. [17] among others, see the survey of DiPrima and Swinney [2]. The present paper follows the approach and notation of Langford et al. [17], and the reader is referred to this work for tables of numerical values and graphs of the neutral stability curves, from which Figs. 3 and 4 have been taken, as well as for details of the numerical procedure used to solve the eigenvalue problem (1.11).

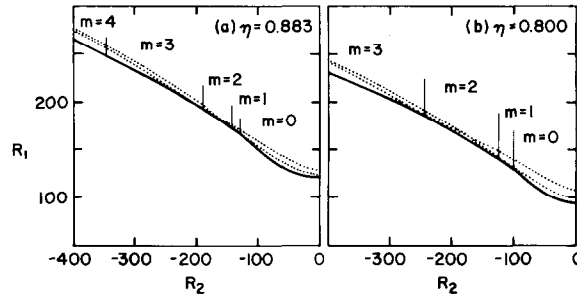


Fig. 3. Neutral stability curves from linear analysis, for counterrotating cylinders. Radius ratios: (a) $\eta = 0.883$ and (b) $\eta = 0.800$.

These linear investigations show that, for each value of the radius ratio η , there are smooth curves in the (R_1, R_2) plane, along which (1.11) has critical eigenvalues, either $\lambda = 0$ (real) or $\lambda = \pm i\omega$ (purely imaginary), see fig. 3. Here m is the azimuthal wave number, defined more precisely below; we note that $\lambda = 0$ if and only if $m = 0$. In every case the eigenvalues have been found to have multiplicity 2, as predicted by symmetry arguments based on the experimental observations in the Introduction.

This paper is concerned with the bicritical points (or codimension-2 points), as in fig. 3, where (1.11) has simultaneously eigenvalues $\lambda = 0$ and $\lambda = \pm i\omega$ (i.e. $m = 0$ and $m \neq 0$ in fig. 3). The analysis shows that, below the envelope of the curves in fig. 3, all the eigenvalues have negative real part, i.e. Couette flow is stable to small disturbances. As R_1 increases in fig. 3, Couette flow loses stability successively to an increasing number of modes (i.e. eigenfunctions of (1.11)). Therefore, intersection points above the lower envelope in fig. 3 are of less interest than those on the envelope, where Couette flow first loses stability. This paper focuses on the intersection of the $m = 0$ and $m = 1$ curves in fig. 3. For a similar study of the intersections of m and $m + 1$ curves with $m > 1$, see Chossat et al. [11].

The bicritical points in fig. 3 move as the radius ratio η varies. However, the numerical analysis in Langford et al. [17] shows that their ordering in R_2 remains monotone, see fig. 4. In section 4 of this paper, we describe the solutions, with their symmetries and stabilities, which bifurcate along the $(m = 0) - (m = 1)$ bicritical curve in fig. 4, in the full nonlinear equations (1.9).

The axial wave number k is determined in different ways by different authors. The approach of Taylor [1] and Langford et al. [17] is to fix R_2 and η , then compute the critical value of R_1 , for which neutral

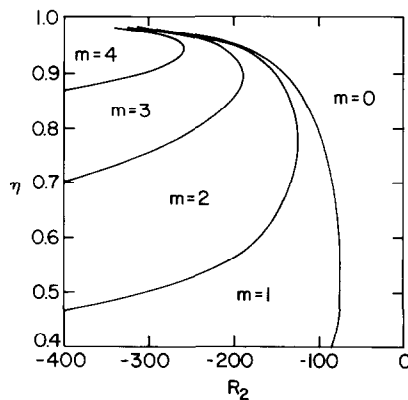


Fig. 4. Curves of bicritical points in the (R_2, η) plane. Between the curves, the primary instability from Couette flow is to a mode with azimuthal wave number m . (Higher wave number modes, not shown, exist in the upper left corner of the figure).

stability ($\text{Re}(\lambda) = 0$) occurs, as a function of k . This function $R_1(k)$ is found to have a global minimum, which uniquely defines R_1^c and k_c for the given η , R_2 and m . It is this critical value R_1^c which is plotted in figs. 3 and 4, see Langford et al. [17] for more details.

A further complication arises when one considers the bicritical points. The critical wave number k_c is in general different on curves with different azimuthal wave numbers m . This means that corresponding eigenfunctions have different periods in z . We wish to assume in the present analysis, as explained in the Introduction, that there is a fixed periodicity in the z direction. Fortunately, the numerical results in Langford et al. [17] show that, for the $(m = 0) - (m = 1)$ bicritical values, the corresponding k_c 's are very close, in fact for moderate gap widths the difference is on the order of 1%, which is comparable to the uncertainty in experiments. Moreover, it is known that as R_1 increases above R_1^c in (1.11) the trivial solution becomes unstable for an entire interval of k values about k_c . This interval grows rapidly, in fact its length has square root dependence on $|R_1 - R_1^c|$. Therefore, very close to a bicritical point (R_2^c, R_1^c) where modes $m = 0$ and $m = 1$ are both neutrally stable but with different values of k_c , there are points (R_2, R_1) where modes with $m = 0$ and $m = 1$ and the *same* values of k are neutrally stable. This common value of k is close to both of the two critical values of k_c , and can be selected in a variety of ways. The calculations reported here used the following procedure for the selection of k_c . Along the $m = 0$ neutral stability curve, the critical wave number $k_{c_0}(R_2) = k_c(R_2)|_{m=0}$ was computed as in Langford et al. [17]. Then in a neighborhood of the former bicritical point, the eigenvalue problem (1.11) was solved for the $m = 1$ mode, using the given $k = k_{c_0}(R_2)$. This yielded a neutral stability curve for $m = 1$, displaced slightly upward from the former curve. Its intersection with the $m = 0$ defined the new bicritical point. In every case the result was only a slight shift of the bicritical point, to larger values of R_1 and more negative values of R_2 . The same procedure appears to have been used by DiPrima et al. [28]. This procedure may be viewed as allowing the axisymmetric Taylor vortex mode to "select" the axial wave number, and then solving for a nonaxisymmetric mode with matching wave number. It makes possible the exploration of mode interactions between modes with the same axial periods. Numerically, the point of intersection was determined by polynomial interpolation, over a mesh of points on which the difference changed sign.

A different approach, used by Chossat et al. [11], is to assume that the cylinder has a finite length l , and minimize over wave numbers k for which l/k is an integer.

Let us now assume that the parameters have been chosen, as determined numerically, so that the eigenvalue problem (1.11) has double eigenvalues at 0 and $\pm i\omega$, and no others on the imaginary axis. As in Langford et al. [17], the corresponding six eigenfunctions can be written

$$\Phi_0 = e^{ikz} \begin{bmatrix} U_0(r) \\ V_0(r) \\ iW_0(r) \end{bmatrix}, \quad \Phi_1 = e^{i(m\theta + kz)} \begin{bmatrix} U_1(r) \\ V_1(r) \\ iW_1(r) \end{bmatrix}, \quad \Phi_2 = e^{i(m\theta - kz)} \begin{bmatrix} U_1(r) \\ V_1(r) \\ -iW_1(r) \end{bmatrix}, \quad (1.12)$$

together with the three complex conjugates. The exponential dependence on z and θ is obtained by elementary separation of variables, then the r -dependent vectors are computed numerically as the solution of an ordinary differential equation two-point boundary value problem. We have chosen to include a factor i in the third components (equivalent to a phase shift of $\pi/4$); this has the consequence that U_0 , V_0 and W_0 are real functions. In every case, U_1 , V_1 and W_1 are complex. Note that m in (1.12) is the azimuthal wave number as in figs. 3 and 4. Henceforth in this paper, we consider only the $m = 1$ nonaxisymmetric modes.

Let us now consider the time-dependent linearized equations, that is (1.9) with the bilinear terms dropped. Again, by separation of variables, this has solutions

$$\phi_0(t, x) = \Phi_0(x), \quad \phi_1(t, x) = e^{-i\omega t}\Phi_1(x), \quad \phi_2(t, x) = e^{-i\omega t}\Phi_2(x), \tag{1.13}$$

together with the 3 complex conjugates. Here $\lambda = -i\omega$ is the numerically computed purely imaginary eigenvalue, and $\omega > 0$. The general real solution of the linearized differential equation is then given by

$$\sum_{j=0}^2 [z_j \phi_j(t, x) + \bar{z}_j \bar{\phi}_j(t, x)], \quad \text{where } z_j \in \mathbb{C}, \tag{1.14}$$

The sum in (1.14) spans a six-dimensional linear space of smooth functions, satisfying the boundary conditions of (1.9), and periodic in t with period $(2\pi/\omega)$. We refer to this space as the *six-dimensional kernel*; it is the space on which the Liapunov–Schmidt reduction of the nonlinear equations will be performed.

Before beginning the Liapunov–Schmidt reduction, we remark that we are seeking time-dependent solutions of the Navier–Stokes equations which exist and are bounded (in fact periodic) for all $t \geq 0$. The corresponding Cauchy problem has been studied by many authors, see for example Sattinger [34], Teman [36] and Iooss [37]. In order to sketch their results, it is convenient to rewrite (1.9) in the form

$$\frac{d\mathbf{u}}{dt} = A(\mu)\mathbf{u} + R_1B(\mathbf{u}, \mathbf{u}), \tag{1.15}$$

where A is the linear part and B is the bilinear part of the right-hand side of (1.9), and μ represents the parameters

$$\mu = (R_1, R_2, \eta) - (R_1^c, R_2^c, \eta^c). \tag{1.16}$$

To find an appropriate function space setting for (1.15), let D denote the physical space between the cylinders, of height $2\pi/k$, and let $L_2(D)$ be the Hilbert space of square-integrable vector functions \mathbf{u} on D , then let $H^j \subset L_2(D)$ be the Sobolev space of \mathbf{u} with partial derivatives square-integrable up to order j and with the inner product

$$(\mathbf{u}, \mathbf{v})_j = \sum_{0 \leq |\alpha| \leq j} \int_D \frac{\partial^{|\alpha|} \mathbf{u}}{\partial x_1^{\alpha_1} \cdots \partial x_3^{\alpha_3}} \cdot \frac{\partial^{|\alpha|} \mathbf{v}}{\partial x_1^{\alpha_1} \cdots \partial x_3^{\alpha_3}} dx. \tag{1.17}$$

Then $H^0 = L_2(D)$ and we define $H_\pi^0 \subset L_2(D)$ to be the subspace of “divergence-free” \mathbf{u} , satisfying

$$0 = \int_D \mathbf{u} \cdot \nabla q dx = \int_{\partial D} q \mathbf{u} \cdot \mathbf{n} d\sigma - \int_D q \nabla \cdot \mathbf{u} dx, \tag{1.18}$$

where $q \in C^1(\bar{D})$, and the second equality holds for sufficiently regular \mathbf{u} (Green’s formula). Thus (1.18) has the effect of incorporating the divergence-free condition and no-flux boundary condition into the function space H_π^0 . Furthermore, H_π^0 is closed in $L_2(D)$ and has orthogonal complement consisting of functions ∇q , $q \in H^1$. Now let π denote the orthogonal projection onto H_π^0 in $L_2(D)$, and project eq.

(1.15) into H_π^0 , to get

$$\frac{d\mathbf{u}}{dt} = \tilde{A}(\mu)\mathbf{u} + R_1\tilde{B}(\mathbf{u}, \mathbf{u}), \tag{1.19}$$

where $\tilde{A} = \pi A$, $\tilde{B} = \pi B$, and the ∇p terms have disappeared. The domain of \tilde{A} is

$$Y = \{ \mathbf{u} \in H_\pi^0 \cap H^2: \mathbf{u} \text{ satisfies B.C.} \}, \tag{1.20}$$

with the inner product of H^2 . Then \tilde{A} is a bounded linear operator from Y to H_π^0 , and the Fredholm alternative holds for \tilde{A} , so that the Liapunov–Schmidt procedure can be applied.

Furthermore, it can be shown that the Cauchy problem has a unique solution on any time interval $[0, T]$, analytic in the parameters μ and analytic for $t \in (0, T)$, provided the initial $\mathbf{u}(0, x) \in Y$ is sufficiently small, see Iooss [37].

In order to apply the Fredholm alternative, we will need the formal adjoint of A which is

$$A^*\mathbf{u} = \begin{bmatrix} \nabla^2 u - \frac{u}{r^2} - \frac{2}{r^2} v_\theta + C(r)u_\theta + 2Dv - p_r \\ \nabla^2 v - \frac{v}{r^2} + \frac{2}{r^2} u_\theta + C(r)v_\theta + 2C(r)u - \frac{1}{r} p_\theta \\ \nabla^2 w + C(r)w_\theta - p_z \end{bmatrix}, \tag{1.21}$$

where $\nabla \cdot \mathbf{u} = 0$, and $\tilde{A}^* = \pi A^*$.

The first step of the Liapunov–Schmidt procedure is a rescaling of the time to fix the (unknown) period in t , by

$$s = (\omega + \tau)t, \tag{1.22}$$

where $i\omega$ is the purely imaginary eigenvalue and τ is a perturbation to be determined. Now (1.9) is equivalent to the nonlinear operator equation

$$N(\mathbf{u}, \mu, \tau) = \tilde{A}(\mu)\mathbf{u} + R_1\tilde{B}(\mathbf{u}, \mathbf{u}) - (\omega + \tau) \frac{d\mathbf{u}}{ds} = 0. \tag{1.23}$$

Note that the Frechet derivative of N is

$$D_u N(0, 0, 0) = \tilde{A}_0 - \omega \frac{d}{ds} \equiv L, \tag{1.24}$$

$$L: C_{2\pi}^1(Y) \rightarrow C_{2\pi}(H_\pi^0),$$

and the kernel of L is spanned by $\{\phi_0, \phi_1, \phi_2, \bar{\phi}_0, \bar{\phi}_1, \bar{\phi}_2\}$, see (1.12)–(1.14). By the Fredholm alternative, the range of L is orthogonal to the kernel of

$$L^* = \tilde{A}_0^* + \omega \frac{d}{ds}, \tag{1.25}$$

and since A^* , given by (1.21), has much the same form as A , the same algorithm can be used to compute a

basis for the kernel of L^* as was used in Langford et al. [17] for the kernel of L . This has the form

$$\begin{aligned} \psi_0(t, x) &= e^{ikz} \begin{bmatrix} U_0^*(r) \\ V_0^*(r) \\ iW_0^*(r) \end{bmatrix}, & \psi_1(t, x) &= e^{i(kz+\theta-\omega t)} \begin{bmatrix} U_1^*(r) \\ V_1^*(r) \\ iW_1^*(r) \end{bmatrix}, \\ \psi_2(t, x) &= e^{i(-kz+\theta-\omega t)} \begin{bmatrix} U_1^*(r) \\ V_1^*(r) \\ -iW_1^*(r) \end{bmatrix}, \end{aligned} \tag{1.26}$$

together with the 3 complex conjugates. The vectors (U_j^*, V_j^*, W_j^*) have been computed numerically, by the method in Langford et al. [17] over the range of parameter values of interest, and normalized so that

$$(\phi_j, \psi_k)_2 = \delta_{jk}, \quad j, k = 0, 1, 2. \tag{1.27}$$

Now we construct a projection P onto $\ker(L)$, along the range of L , given by

$$P\mathbf{u} = \sum_{j=0}^2 [(\mathbf{u}, \psi_j)_2 \phi_j + (\mathbf{u}, \bar{\psi}_j)_2 \bar{\phi}_j], \tag{1.28}$$

where $P\mathbf{u}$ is real, since \mathbf{u} is real. Applying P to (1.23) gives the alternative problems

$$PN(\mathbf{u}, \mu, \tau) = 0, \tag{1.29}$$

$$(I - P)N(\mathbf{u}, \mu, \tau) = 0, \tag{1.30}$$

and we similarly decompose \mathbf{u} into its projection in $\ker(L)$ and in the orthogonal complement to $\ker(L^*)$

$$\mathbf{u} = \sum_{j=0}^2 (z_j \phi_j + \bar{z}_j \bar{\phi}_j) + \mathbf{W}, \tag{1.31}$$

where $\mathbf{z} = (z_0, z_1, z_2) \in \mathbb{C}^3$, and $P\mathbf{W} = 0$. By the Implicit Function Theorem, we can solve (1.30) uniquely near $(0, 0, 0)$ for

$$\mathbf{W} = \mathbf{W}(\mathbf{z}, \bar{\mathbf{z}}, \mu, \tau). \tag{1.32}$$

Substituting this into (1.29) gives the 6-dimensional nonlinear bifurcation equation

$$G(\mathbf{z}, \bar{\mathbf{z}}, \mu, \tau) \equiv PN\left(\sum_j (z_j \phi_j + \bar{z}_j \bar{\phi}_j) + \mathbf{W}(\mathbf{z}, \bar{\mathbf{z}}, \mu, \tau)\right) = 0, \tag{1.33}$$

which has 6 components

$$g^j = (N, \psi_j)_2, \quad h^j = (N, \bar{\psi}_j)_2, \quad j = 0, 1, 2. \tag{1.34}$$

However, since \mathbf{u} is real, $h^j = \bar{g}^j$, so only the first three need be considered, and we rewrite (1.33) in

components as

$$G: \mathbb{C}^3 \times \mathbb{C}^3 \times \mathbb{R}^3 \times \mathbb{R} \rightarrow \mathbb{C}^3, \quad (1.35)$$

where

$$G(z, \bar{z}, \mu, \tau) = \begin{bmatrix} g^0 \\ g^1 \\ g^2 \end{bmatrix} = \begin{bmatrix} 0 \\ 0 \\ 0 \end{bmatrix}. \quad (1.36)$$

In the next section we show how the form of G is determined by the $O(2) \times SO(2)$ symmetry which the bifurcation equation inherits from the original problem.

2. Symmetry and normal form analysis

The eigenfunctions of the Navier–Stokes equations linearized about Couette flow at the bicritical point where steady-state/Hopf mode interactions occur were given in (1.12) and (1.13). As in (1.14) we coordinatize the six-dimensional center subspace by $(z_0, z_1, z_2) \in \mathbb{C}^3 \cong \mathbb{R}^6$.

Using (1.12)–(1.14) we can compute how the symmetries of the Taylor–Couette apparatus act on \mathbb{C}^3 . In this calculation we set

$$\begin{aligned} \text{(a)} \quad Z &= kz, \\ \text{(b)} \quad \Theta &= \theta - \omega t. \end{aligned} \quad (2.1)$$

The group $O(2)$ of axial translations and flips is generated by

$$\begin{aligned} \text{(a)} \quad S_\phi(Z, \Theta) &= (Z + \phi, \Theta), \\ \text{(b)} \quad \kappa(Z, \Theta) &= (-Z, \Theta), \end{aligned} \quad (2.2)$$

where, in addition, κ changes the sign of the third component of the velocity field. It follows that S_ϕ and κ induce actions on \mathbb{C}^3 by

$$\begin{aligned} \text{(a)} \quad S_\phi(z_0, z_1, z_2) &= (e^{i\phi}z_0, e^{i\phi}z_1, e^{-i\phi}z_2), \\ \text{(b)} \quad \kappa(z_0, z_1, z_2) &= (\bar{z}_0, z_2, z_1). \end{aligned} \quad (2.3)$$

The group $SO(2)$ of azimuthal rotations acts by

$$T_\theta(Z, \Theta) = (Z, \Theta + \theta) \quad (2.4)$$

and induces the action on \mathbb{C}^3

$$T_\theta(z_0, z_1, z_2) = (z_0, e^{i\theta}z_1, e^{i\theta}z_2). \quad (2.5)$$

The reduced bifurcation equations obtained by the Liapunov–Schmidt reduction described in section 1 commute with the action of $O(2) \times SO(2)$ on \mathbb{C}^3 defined by (2.3) and (2.5). The consequences of this

symmetry for these reduced equations is summarized in the remainder of this section, which is divided into four subsections:

- 2.1. The general form for mappings on \mathbb{C}^3 which commute with $O(2) \times SO(2)$.
- 2.2. The stationary and periodic solutions found in this mode interaction.
- 2.3. The asymptotic stability of these solutions.
- 2.4. Possible bifurcations to tori.

2.1. $O(2) \times SO(2)$ invariants and equivariants

The restrictions placed on the reduced equations by symmetry were first given by Golubitsky and Stewart [4] and in improved form using the coordinates described above by Langford [38]. A complete proof may be found in Golubitsky et al. [10], ch. XX, §2.

Let

- (a) $\rho = |z_0|^2$,
- (b) $N = |z_1|^2 + |z_2|^2$,
- (c) $\delta = |z_2|^2 - |z_1|^2$,
- (d) $\Delta = \delta^2$,
- (e) $A = z_0^2 \bar{z}_1 z_2$,
- (f) $\Phi = \text{Re } A$,
- (g) $\Psi = \delta \text{Im } A$.

(2.6)

Theorem 2.1. Every smooth $O(2) \times SO(2)$ invariant function germ $f: \mathbb{C}^3 \rightarrow \mathbb{R}$ has the form

$$f(z_0, z_1, z_2) = h(\rho, N, \Delta, \Phi, \Psi)$$

for some smooth function germ $h: \mathbb{R}^5 \rightarrow \mathbb{R}$.

Theorem 2.2. Let $g: \mathbb{C}^3 \times \mathbb{R}^k \rightarrow \mathbb{C}^3$ be $O(2) \times SO(2)$ -equivariant. Then g has the form

$$\begin{aligned}
 g(z, \mu) = & (c^1 + i\delta c^2) \begin{bmatrix} z_0 \\ 0 \\ 0 \end{bmatrix} + (c^3 + i\delta c^4) \begin{bmatrix} \bar{z}_0 z_1 \bar{z}_2 \\ 0 \\ 0 \end{bmatrix} \\
 & + (p^1 + iq^1) \begin{bmatrix} 0 \\ z_1 \\ z_2 \end{bmatrix} + (p^2 + iq^2) \delta \begin{bmatrix} 0 \\ z_1 \\ -z_2 \end{bmatrix} \\
 & + (p^3 + iq^3) \begin{bmatrix} 0 \\ z_0^2 z_2 \\ \bar{z}_0^2 z_1 \end{bmatrix} + (p^4 + iq^4) \delta \begin{bmatrix} 0 \\ z_0^2 z_2 \\ -\bar{z}_0^2 z_1 \end{bmatrix},
 \end{aligned}$$

(2.7)

where c^j , p^j and q^j are functions of ρ , N , Δ , Φ , Ψ and μ .

2.2. Stationary and periodic solutions

Let $g(z, \mu, \tau)$ be the reduced mapping obtained by the Liapunov–Schmidt reduction in section 1 where $z = (z_0, z_1, z_2) \in \mathbb{C}^3$, $\mu = (R_1, R_2, \eta) \in \mathbb{R}^3$ and $\tau \in \mathbb{R}$. The parameters μ refer to the system parameters, whereas τ is the perturbed period parameter introduced in the reduction procedure. In this section we explain how to solve $g = 0$, using the fact that g must have the form (2.7), where the c^j, p^j, q^j depend on μ and τ as well as the basic $O(2) \times SO(2)$ invariants.

Our method involves classifying (up to conjugacy) the isotropy subgroups Σ of the action of $O(2) \times SO(2)$ on \mathbb{C}^3 and then considering the restricted system of equations

$$g|_{\text{Fix}(\Sigma) \times \mathbb{R}^3 \times \mathbb{R}} = 0,$$

where the *fixed point subspace* is defined by

$$\text{Fix}(\Sigma) = \{z \in \mathbb{C}^3: \sigma z = z \ \forall \sigma \in \Sigma\}. \tag{2.8}$$

Proofs of these results may be found in Golubitsky and Stewart [4] and Golubitsky et al. [10], ch. XX.

Define the subgroups of $O(2) \times SO(2)$

- (a) $\widetilde{SO}(2) = \{(\phi, -\phi): \phi \in SO(2)\}$,
 - (b) $Z_2(\kappa) = \{1, \kappa\}$,
 - (c) $Z_2^c = \{1, (\pi, \pi)\}$,
 - (d) $Z_2(\kappa \cdot (\pi, \pi)) = \{1, \kappa \cdot (\pi, \pi)\}$.
- (2.9)

Let Δ and Σ be subgroups. We use the notation $\Delta \rightarrow \Sigma$ when some subgroup conjugate to Δ is contained in Σ .

Theorem 2.3. The lattice of isotropy subgroups of $O(2) \times SO(2)$ is given in table I.

Recall that equivariance implies that fixed point subspaces are invariant subspaces of g . Thus, in table II we list the isotropy subgroups, the experimentally observed states whose symmetries correspond to these isotropy subgroups, (group) orbit representatives in the fixed point subspaces and the equations $g = 0$ restricted to these orbit representatives.

We note that generically in two-parameter families the equation $g = 0$ has no solutions with isotropy Z_2^c or $\{1\}$ and these isotropy subgroups have been omitted from table II. We also note that in the Liapunov–Schmidt reduction all linear terms must vanish. Thus

$$c^1(0) = p^1(0) = q^1(0) = 0.$$

Table I
Lattice of isotropy subgroups of $O(2) \times SO(2)$ acting in \mathbb{C}^3 .

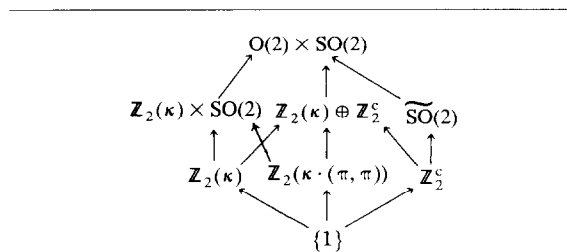


Table II
Branching equations.

| Isotropy subgroup | Observed states | Orbit representatives | $g \text{Fix}(\Sigma) \times \mathbb{R}^k$ |
|--|------------------|------------------------|---|
| (a) $O(2) \times SO(2)$ | Couette flow | $z = 0$ | — |
| (b) $\mathbf{Z}_2(\kappa) \times SO(2)$ | Taylor vortices | $(x, 0, 0), x > 0$ | $c^1 = 0$ |
| (c) $\widetilde{SO}(2)$ | spiral vortices | $(0, a, 0), a > 0$ | $p^1 - a^2 p^2 = 0$ $q^1 - a^2 q^2 = 0$ |
| (d) $\mathbf{Z}_2(\kappa) \oplus \mathbf{Z}_2^c$ | ribbons | $(0, a, a), a > 0$ | $p^1 = 0$ $q^1 = 0$ |
| (e) $\mathbf{Z}_2(\kappa \cdot (\pi, \pi))$ | wavy vortices | $(iy, a, a), a, y > 0$ | $c^1 - a^2 c^3 = 0$ $p^1 - y^2 p^3 = 0$ $q^1 - y^2 q^3 = 0$ |
| (f) $\mathbf{Z}_2(\kappa)$ | twisted vortices | $(x, a, a), a, x > 0$ | $c^1 + a^2 c^3 = 0$ $p^1 + x^2 p^3 = 0$ $q^1 + x^2 q^3 = 0$ |

In addition, the Liapunov–Schmidt reduction implies

$$c^1_\tau(0) = p^1_\tau(0) = 0, \quad q^1_\tau(0) \neq 0.$$

Thus, the equations involving the q 's in entries (c)–(f) may be solved implicitly for τ .

Later we will work explicitly with g truncated at third order in z and linear order in the parameters. Then we will assume that the c^j, p^j and q^j have the form:

$$\begin{aligned}
 c^1 &= c^1_\mu(0)\mu + c^1_\rho(0)\rho + c^1_N(0)N, \\
 c^2 &= c^2(0), \\
 c^3 &= c^3(0), \\
 c^4 &= 0, \\
 p^1 &= p^1_\mu(0)\mu + p^1_\rho(0)\rho + p^1_N(0)N, \\
 q^1 &= q^1_\mu(0)\mu + q^1_\rho(0)\rho + q^1_N(0)N, \\
 p^2 &= p^2(0), \\
 q^2 &= q^2(0), \\
 p^3 &= p^3(0), \\
 q^3 &= q^3(0), \\
 p^4 &= 0, \\
 q^4 &= 0.
 \end{aligned} \tag{2.10}$$

As shown in Golubitsky and Stewart [4], the existence of solutions (a)–(e) in table II are determined at third order, assuming certain nondegeneracy conditions and moreover, these solution branches do not depend on τ .

2.3. Asymptotic stability

Chossat and Golubitsky [24] show that to third order the Liapunov–Schmidt reduction with τ set to 0 is precisely the same as the Poincaré–Birkhoff normal form of the center manifold vector field. Now in equivariant Hopf bifurcation a vector field is in normal form precisely when it commutes with S^1 phase shift symmetry (cf. Golubitsky and Stewart [39] and Elphich et al. [40]). It follows from (2.1)(b) that the phase shift symmetry (after scaling ω to be unity) acts identically with the azimuthal rotation symmetry. Thus, the actions of S^1 and $SO(2)$ are identical on \mathbb{C}^3 and the center manifold vector field is, in this case, automatically in Poincaré–Birkhoff normal form.

Thus when the signs of the eigenvalues of $dg|_{g=0}$ are determined at third order, the asymptotic stability and instability of the solution $g=0$ is also determined. As discussed in detail in Golubitsky and Stewart [4] and Golubitsky et al. [10], restrictions on dg induced by symmetry from the isotropy subgroup are often sufficient to enable one to calculate the individual eigenvalues of dg . For each of the solutions in table II (a)–(d) this scenario is possible to complete and the results are listed in table III. For wavy and twisted vortices however, the computation of the eigenvalues of dg reduces to determining the eigenvalues of two 2×2 matrices. The entries of these matrices are complicated functions of the normal form equations. So in table III (e)–(f) we list only the contribution to the matrix entries stemming from terms of degree ≤ 3 in g .

2.4. Bifurcation to tori

There are several possible bifurcations to tori indicated by the entries in table III. These tori will bifurcate from the branches of either spiral vortices, wavy vortices or twisted vortices. (The possible Hopf bifurcations along the branch of Taylor vortices just indicate bifurcations to the branches of the time periodic wavy and twisted vortices states.)

Along the branch of spirals the eigenvalue c^1 typically changes sign and when this happens a Hopf bifurcation to solutions on an invariant 2-torus occurs. Crawford et al. [41] show that the direction of branching, and hence the asymptotic stability, of these 2-frequency solutions can be determined from the third order terms in the bifurcation equations, g . Specifically, this branch of 2-tori is asymptotically stable when the remaining eigenvalues along the spiral vortices are negative and when

$$h = c_p^1 - \frac{p_\rho^1 c_N^1}{2(p_N^1 - p^2)} - \frac{c^3}{2} \operatorname{Re} \left[\frac{p^3 - iq^3}{p^2 + i(c^2 - q^2)} \right] \quad (2.11)$$

is negative.

Along the branch of wavy vortices each of the 2×2 matrices can undergo a Hopf bifurcation. Purely imaginary eigenvalues in the first matrix indicate a Hopf bifurcation in the fixed point subspace of $\mathbb{Z}_2(\kappa \cdot (\pi, \pi))$; thus the resulting solutions will have the same symmetries as wavy vortices for all time. This 2-frequency motion can be identified with the observed state of modulated wavy vortices.

In principle a Hopf bifurcation can occur by complex conjugate eigenvalues of the second 2×2 matrix crossing the imaginary axis along the branch of wavy vortices. Results of Chossat and Golubitsky [46] prove that the resulting flow will have three independent frequencies: one near the frequency of spiral vortices, one near the frequency determined by the imaginary eigenvalues of one Hopf bifurcation, and one near 0, corresponding to a slow drift in the axial direction. To our knowledge a flow having these characteristics has not been observed in the Taylor–Couette system.

Table III
Computation asymptotic stability.

| State | Amplitude equations | Signs of eigenvalues |
|----------------------|--|---|
| (a) Couette flow | -- | c^1 (twice) p^1 (four times) |
| (b) Taylor vortices | $c^1 = 0$ | c_p^1 $p^1 + x^2 p^3$ (twice)* $p^1 - x^2 p^3$ (twice)* 0 |
| (c) Spiral vortices | $p^1 - a^2 p^2 = 0$ | c^1 (twice)* p^2 (twice)* $p_N^1 - p^2 + (2p_\Delta^1 - p_N^2)a^2 - 2p_\Delta^2 a^4$ 0 |
| (d) Ribbons | $p^1 = 0$ | $c^1 + a^2 c^3$ $c^1 - a^2 c^3$ p_N^1 $-p^2$ 0 (twice) |
| (e) Wavy vortices | $c^1 - a^2 c^3 = 0$ $p^1 - y^2 p^3 = 0$ | 0 (twice) ev's of $\begin{bmatrix} c_p^1 y^2 & (2c_N^1 - c^3) ay \\ (p_p^1 - p^3) ay & 2p_N^1 a^2 \end{bmatrix}$ ev's of $\begin{bmatrix} p^3 y^2 - 2p^2 a^2 & -q^3 y^2 \\ 2(c^2 - q^2)a^2 + q^3 y^2 & c^3 a^2 + p^3 y^2 \end{bmatrix}$ |
| (f) Twisted vortices | $c^1 + a^2 c^3 = 0$ $p^1 + x^2 p^3 = 0$ | 0 (twice) ev's of $\begin{bmatrix} c_p^1 x^2 & (2c_N^1 + c^3) ax \\ (p_p^1 + p^3) ax & 2p_N^1 a^2 \end{bmatrix}$ ev's of $-\begin{bmatrix} p^3 x^2 + 2p^2 a^2 & -q^3 x^2 \\ -2(c^2 - q^2)a^2 + q^3 x^2 & p^3 x^2 + c^3 a^2 \end{bmatrix}$ |

*Each of these double eigenvalues are in fact the real part of eigenvalues associated to a 2×2 rotation matrix. Thus Hopf bifurcations are associated with these eigenvalues crossing through 0.

Thirdly, in principle it is possible for a single eigenvalue of the second matrix to go through 0. The resulting bifurcating flow will have 2-frequencies with one near 0. This observation also follows from the methods in Chossat and Golubitsky [46].

Analogous torus bifurcations can occur along the branch of twisted vortices. In all, there are seven distinct branches of tori that could occur as secondary and tertiary bifurcations resulting from this steady

state/Hopf mode interaction. Which ones do actually occur depends on the exact values of the Taylor coefficients listed in (2.10). Determination of the direction of branching and the asymptotic stabilities of the tertiary branches of tori bifurcating from wavy and twisted vortices may require terms of degree 5 and higher in the Taylor expansion of g , and this issue is not considered here.

3. Computation of the coefficients

The previous section ascertained the possible solutions of the bifurcation equations, according to their symmetries, and determined which cubic order coefficients in the normal form are required to decide the direction of branching and the stability of the solutions, up to secondary bifurcations. This section describes how these coefficients have been computed, from the Navier–Stokes equations, over the range of parameter values of interest.

First we express the required derivatives of the invariant functions appearing in (2.10) in terms of derivatives of the bifurcation function defined in section 1. Subscripts denote partial derivatives, and all derivatives are evaluated at the origin:

$$\begin{aligned}
 \text{(a)} \quad c_R^1 &= \operatorname{Re}\left(g_{z_0 R}^0\right), \quad R = R_1 \text{ or } R_2, \\
 \text{(b)} \quad c_\rho^1 &= \operatorname{Re}\left(g_{z_0 z_0 \bar{z}_0}^0\right)/2, \\
 \text{(c)} \quad c_N^1 &= \operatorname{Re}\left(g_{z_0 z_2 \bar{z}_2}^0\right), \\
 \text{(d)} \quad c^2 &= \operatorname{Im}\left(g_{z_0 z_2 \bar{z}_2}^0\right), \\
 \text{(e)} \quad c^3 &= \operatorname{Re}\left(g_{\bar{z}_0 z_1 \bar{z}_2}^0\right), \\
 \text{(f)} \quad p_R^1 &= \operatorname{Re}\left(g_{z_1 R}^1\right), \quad R = R_1 \text{ or } R_2, \\
 \text{(g)} \quad p_\rho^1 &= \operatorname{Re}\left(g_{z_0 \bar{z}_0 z_1}^1\right), \\
 \text{(h)} \quad p_N^1 &= \operatorname{Re}\left(g_{z_1 z_2 \bar{z}_2}^1\right)/2 + \operatorname{Re}\left(g_{z_1 z_1 \bar{z}_1}^1\right)/4, \\
 \text{(i)} \quad p^2 &= \operatorname{Re}\left(g_{z_1 z_2 \bar{z}_2}^1\right)/2 - \operatorname{Re}\left(g_{z_1 z_1 \bar{z}_1}^1\right)/4, \\
 \text{(j)} \quad q^2 &= \operatorname{Im}\left(g_{z_1 z_2 \bar{z}_2}^1\right)/2 - \operatorname{Im}\left(g_{z_1 z_1 \bar{z}_1}^1\right)/4, \\
 \text{(k)} \quad p^3 &= \operatorname{Re}\left(g_{z_0 z_0 z_2}^1\right)/2, \\
 \text{(l)} \quad q^3 &= \operatorname{Im}\left(g_{z_0 z_0 z_2}^1\right)/2.
 \end{aligned} \tag{3.1}$$

The R_1 and R_2 derivatives are then obtained by differentiation of the equations defining g^0 and g^1 ,

$$c_R^1 = \operatorname{Re}\langle A_R(0)\phi_0, \psi_0 \rangle, \quad p_R^1 = \operatorname{Re}\langle A_R(0)\phi_0, \psi_1 \rangle, \tag{3.2}$$

where $R = R_1$ or R_2 and $A(\mu)$ is as in (1.15). Here the angle brackets denote inner products which are in

fact the L_2 integrals of section 1, defined by

$$\begin{aligned} \langle \mathbf{u}, \mathbf{v} \rangle &= \iiint_D \mathbf{v}^* \mathbf{u} \, d^3x \\ &= \frac{1}{2\pi} \int_0^{2\pi} \frac{k}{2\pi} \int_0^{2\pi/k} \int_a^b \mathbf{v}^* \mathbf{u} \, dr \, dz \, d\theta. \end{aligned} \tag{3.3}$$

The integrals were all evaluated numerically, using Simpson’s rule, from previously computed and tabulated values of the eigenfunctions ϕ_j and adjoint eigenfunctions ψ_j . The method of calculation of these eigenfunctions is described in Langford et al. [17].

Similarly the formulas for the cubic coefficients are obtained by differentiation of the bifurcation equation (1.36) or (1.33), but in this case z -derivatives of W appear, and so it is necessary to solve (1.30) for W to second order. In general, we find

$$g_{z_k z_l z_m}^j = R_1 \left\langle \hat{B}(W_{z_k z_l}, \phi_m) + \hat{B}(W_{z_k z_m}, \phi_l) + \hat{B}(W_{z_m z_l}, \phi_k), \psi_j \right\rangle, \tag{3.4}$$

where $W_{z_k z_l}$ is the solution of

$$LW_{z_k z_l} + R_1 \hat{B}(\phi_k, \phi_l) = 0 \tag{3.5}$$

and \hat{B} denotes the symmetric bilinear form

$$\hat{B}(u, v) = B(u, v) + B(v, u). \tag{3.6}$$

Numerically, this problem was solved as follows. First the linear term $\hat{B}(\phi_k, \phi_l)$ in (3.5) was evaluated using tabulated values of the eigenfunctions. Then the nonhomogeneous boundary value problem (3.5) was solved for $W_{z_k z_l}$, using a slightly modified version of the shooting algorithm used previously to compute the eigenfunctions. Finally, the inner products (3.4) were computed, using Simpson’s rule.

All of the computations described here were performed on microcomputers of the IBM PC class, in the BASIC programming language. This may be compared with a direct numerical solution of the original fluid dynamical equations, which though possible, would require a supercomputer and more sophisticated programming techniques.

4. Results and conclusions

The results of the numerical calculations are presented in tables IV, V and VI. These data were used to plot bifurcation diagrams, shown in figs. 5 and 6. The radius ratios η were chosen in the range $0.43 \leq \eta \leq 0.98$, with special emphasis on the values $\eta = 0.736$ and $\eta = 0.883$ for which experimental data are available (Andereck et al. [3], Tagg et al. [5]).

Table IV presents some results of the linear stability analysis, and for comparison purposes, calculations of Langford et al. [17] indicated by *. (The symbols are as defined in section 1, except for k_0^* and k_1^* which are the axial wave numbers computed independently for the $m = 0$ and $m = 1$ modes. The azimuthal wave speed ω is in units of Ω_1 .) Recall from section 1 that the two axial wave numbers, for the $m = 0$ and $m = 1$ modes, have been forced to have the identical value k in this paper. As a result, the minimizing value of R_1 can be expected to be larger here than in Langford et al. [17], and the other parameters will be perturbed similarly. Table IV shows that the changes are large for $\eta \leq 0.6$, but are smaller for larger η (generally less than experimental uncertainties). Therefore, the simple procedure employed to select k , in this paper seems to be justified for moderate and narrow gaps, but would have to be modified for wider gaps.

Table IV
Parameter values at bicriticality, linear stability analysis.

| η | 0.430 | 0.500 | 0.600 | 0.736 | 0.800 | 0.850 | 0.870 | 0.883 | 0.900 | 0.950 | 0.970 | 0.980 |
|------------|---------|--------|---------|--------|---------|--------|---------|--------|---------|--------|---------|---------|
| R_2 | -92.19 | -76.13 | 75.57 | -87.47 | 99.29 | 114.08 | 122.40 | 128.95 | 139.42 | 197.21 | 254.74 | 312.11 |
| R_2^* | -79.14 | -73.79 | -75.03 | -87.71 | 99.25 | 114.06 | 122.38 | 128.93 | 139.41 | 197.17 | -254.68 | 311.98 |
| R_1 | 103.70 | 96.49 | 98.96 | 114.69 | 129.57 | 148.16 | 158.63 | 166.89 | 180.10 | 253.27 | 326.39 | 399.42 |
| R_1^* | 97.51 | 95.25 | 98.67 | 114.82 | 129.55 | 148.15 | 158.62 | 166.88 | 180.09 | 253.26 | 326.36 | 399.35 |
| k | 4.668 | 4.131 | 3.829 | 3.631 | 3.573 | 3.536 | 3.524 | 3.517 | 3.507 | 3.483 | 3.474 | 3.470 |
| k_0^* | 4.409 | 4.079 | 3.816 | 3.631 | 3.571 | 3.536 | 3.524 | 3.516 | 3.507 | 3.483 | 3.474 | 3.470 |
| k_1^* | 3.950 | 3.813 | 3.692 | 3.590 | 3.551 | 3.526 | 3.517 | 3.511 | 3.503 | 3.482 | 3.474 | 3.470 |
| ω | 0.2748 | 0.2861 | 0.3093 | 0.3353 | 0.3450 | 0.3516 | 0.3539 | 0.3554 | 0.3573 | 0.3623 | 0.3641 | 0.3649 |
| ω^* | 0.2622 | 0.2813 | 0.3075 | 0.3345 | 0.3445 | 0.3514 | 0.3535 | 0.3546 | 0.3569 | 0.3621 | 0.3638 | 0.3646 |
| μ | -0.3823 | 0.3945 | -0.4582 | 0.5613 | -0.6130 | 0.6545 | -0.6713 | 0.6823 | -0.6967 | 0.7397 | 0.7571 | -0.7658 |
| μ^* | -0.3490 | 0.3874 | -0.4563 | 0.5622 | -0.6129 | 0.6544 | 0.6712 | 0.6822 | 0.6967 | 0.7396 | 0.7569 | -0.7656 |

*Values from Langford et al. [17]

Table V
Linear and cubic bifurcation coefficients

| n | 0.430 | 0.500 | 0.600 | 0.736 | 0.800 | 0.850 | 0.870 | 0.883 | 0.900 | 0.950 | 0.970 | 0.980 |
|-------------|-----------|-----------|-----------|-----------|-----------|-----------|-----------|-----------|-----------|-----------|-----------|-----------|
| $c_{R_1}^1$ | +9.72E-01 | +8.29E-01 | +3.84E-01 | +5.37E-01 | +4.57E-01 | +3.90E-01 | +3.61E-01 | +3.42E-01 | +3.14E-01 | +2.19E-01 | +1.69E-01 | +1.38E-01 |
| $c_{R_2}^1$ | +4.41E-01 | +4.36E-01 | +6.98E-01 | +2.94E-01 | +2.48E-01 | +2.09E-01 | +1.93E-01 | +1.82E-01 | +1.67E-01 | +1.15E-01 | +8.81E-02 | +7.16E-02 |
| c_p^1 | -9.93E+02 | -4.70E+02 | -1.80E+02 | -3.92E+01 | -1.34E+01 | -2.68E+00 | -1.46E+01 | +1.06E+00 | +2.16E+00 | +2.70E+00 | -1.96E+00 | +1.41E+00 |
| c_N^1 | -2.36E+03 | -1.22E+03 | -5.37E+02 | -1.64E+02 | -8.44E+01 | -4.50E+01 | -3.36E+01 | -2.72E+01 | -2.01E+01 | -5.92E+00 | -2.67E+00 | -1.50E+00 |
| c^2 | -1.64E+03 | -8.47E+02 | -4.29E+02 | -1.68E+02 | -9.79E+01 | -5.82E+01 | -4.54E+01 | -3.79E+01 | -2.91E+01 | -9.44E+00 | -4.24E+00 | -2.27E+00 |
| c^3 | -1.96E+03 | -1.00E+03 | -4.67E+02 | -1.69E+02 | -9.92E+01 | -6.16E+01 | -4.97E+01 | -4.28E+01 | -3.45E+01 | -1.47E+01 | -8.33E+00 | -5.41E+00 |
| $p_{R_1}^1$ | +7.58E-01 | +6.55E-01 | +5.88E-01 | +4.88E-01 | +4.29E-01 | +3.73E-01 | +3.48E-01 | +3.30E-01 | +3.05E-01 | +2.16E-01 | +1.68E-01 | +1.37E-01 |
| $p_{R_2}^1$ | +2.94E-01 | +2.71E-01 | +2.61E-01 | +2.33E-01 | +2.10E-01 | +1.86E-01 | +1.74E-01 | +1.66E-01 | +1.54E-01 | +1.11E-01 | +8.63E-02 | +7.06E-02 |
| p_p^1 | -1.69E+03 | -8.42E+02 | -3.82E+02 | -1.23E+02 | -6.41E+01 | -3.46E+01 | -2.60E+01 | -2.11E+01 | -1.57E+01 | -4.84E+00 | -2.27E+00 | -1.32E+00 |
| p_N^1 | -1.41E+03 | -7.42E+02 | -3.35E+02 | -1.01E+02 | -4.98E+01 | -2.46E+01 | -1.75E+01 | 1.36E+01 | -9.34E+00 | -1.70E+00 | -3.83E-01 | -5.41E-02 |
| q^1 | -2.78E+02 | -1.65E+02 | -8.58E+01 | -3.50E+01 | -2.19E+01 | -1.42E+01 | -1.17E+01 | -1.02E+01 | -8.31E+00 | -3.65E+00 | -2.08E+00 | -1.35E+00 |
| q^2 | -1.01E+03 | -4.98E+02 | -2.57E+02 | -1.04E+02 | -6.19E+01 | -3.73E+01 | -2.92E+01 | -2.45E+01 | -1.89E+01 | -6.26E+00 | -2.84E+00 | -1.53E+00 |
| q^3 | -9.66E+02 | -4.99E+02 | -2.45E+02 | -9.43E+01 | -5.65E+01 | -3.53E+01 | -2.85E+01 | -2.44E+01 | -1.96E+01 | -8.04E+00 | -4.43E+00 | -2.82E+00 |
| q^3 | -2.65E+02 | -1.59E+02 | -1.05E+02 | -5.12E+01 | -3.20E+01 | -1.98E+01 | -1.57E+01 | -1.32E+01 | -1.02E+01 | -3.37E+00 | -1.52E+00 | -8.14E-01 |

Table VI
Coefficients for direction and stability of bifurcation, as defined in (4.1), except MSP defined in (2.11).

| η | 0.430 | 0.500 | 0.600 | 0.736 | 0.800 | 0.850 | 0.870 | 0.883 | 0.900 | 0.950 | 0.970 | 0.980 |
|--------|-----------|-----------|-----------|-----------|-----------|-----------|-----------|-----------|-----------|-----------|-----------|-----------|
| (a) | -9.93E+02 | -4.70E+02 | -1.80E+02 | 3.92E+01 | 1.34E+01 | -2.68E+00 | -1.46E-01 | -1.06E+00 | +2.16E+00 | +2.70E+00 | +1.96E+00 | +1.41E+00 |
| (c) | -1.83E+03 | -8.04E+02 | -3.31E+02 | 9.73E+01 | 4.94E+01 | -2.63E+01 | -1.96E+01 | -1.59E+01 | -1.18E+01 | -3.41E+00 | -1.46E+00 | -7.65E-01 |
| (d) | +4.59E+01 | +2.32E+01 | +1.08E+01 | +3.92E+00 | +2.27E+00 | +1.29E+00 | +9.63E-01 | +7.74E-01 | +5.56E-01 | +1.18E-01 | +3.56E-02 | +1.34E-02 |
| (g) | -2.32E-03 | -1.02E-03 | -4.39E-02 | -1.34E-02 | -6.93E-01 | -3.73E-01 | -2.80E-01 | -2.28E+01 | -1.69E+01 | -5.00E+00 | -2.16E+00 | -1.14E+00 |
| (h) | +6.57E+02 | +2.93E+02 | +1.11E+02 | +3.09E+01 | +1.58E+01 | -8.61E+00 | +6.57E+00 | +5.42E+00 | +4.12E+00 | +1.37E+00 | +6.32E-01 | -3.46E-01 |
| (j) | -1.13E+03 | -5.78E+02 | -2.49E+02 | -6.63E+01 | -2.79E+01 | -1.04E+01 | 5.77E-00 | -3.42E+00 | -1.04E+00 | +1.95E+00 | +1.70E+00 | +1.30E+00 |
| (k) | -6.86E+02 | -3.19E+02 | -1.42E+02 | -4.46E+01 | -2.34E+01 | -1.27E+01 | -9.59E+00 | 7.82E+00 | -5.82E+00 | -1.71E+00 | -7.35E-01 | -3.84E-01 |
| (l) | -1.50E+07 | -3.92E+06 | -8.45E+05 | -1.00E+05 | -3.10E+04 | -1.05E+04 | -6.36E+03 | 4.46E+03 | 2.68E+03 | 3.51E+02 | -9.31E-01 | -3.50E+01 |
| (m) | +8.02E+05 | +2.06E+05 | +3.81E+04 | +3.42E+03 | +8.06E+02 | +1.53E+02 | +4.91E+01 | +9.63E+00 | -1.82E+01 | -1.83E+01 | -7.96E+00 | -3.78E+00 |
| MSP | +2.74E+03 | +1.40E-03 | +6.60E+02 | +2.65E+02 | +1.83E+02 | +1.52E+02 | +1.56E+02 | +1.75E+02 | +3.13E+02 | -6.14E+00 | +3.07E-00 | +3.54E+00 |

The tables contain no entries for $\eta < 0.43$, for the following reason. If k_1 is forced to be equal to k_0 , the critical stability curves for the $m = 1$ and $m = 0$ modes can have two points of intersection. For example, when $\eta = 0.45$ the second crossing is near $(R_2, R_1) = (-145, 125)$. As η decreases, these two bicritical points come together, then coalesce and disappear, between $\eta = 0.425$ and $\eta = 0.420$. For $\eta \leq 0.420$, no bicritical points were found. This appears to be an artifact of the procedure used to select k ; when k_0 and k_1 were minimized independently, Langford et al. [17] found only a unique bicritical point. However, the region $\eta < 0.4$ remains largely unexplored.

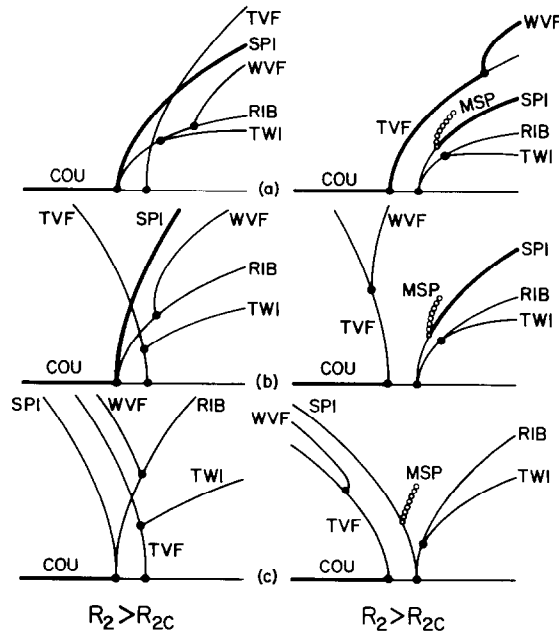


Fig. 5. Bifurcation diagrams for increasing R_1 , with R_2 constant on each side of R_{2c} , and for radius ratios: (a) $\eta = 0.736$, (b) $\eta = 0.883$, (c) $\eta = 0.950$. Thick lines represent stable branches, thin lines are unstable, and circles represent quasiperiodic solution branches.

All of the parameters in table IV are experimentally measurable in the laboratory. See Langford et al. [17] for corresponding experimental data at radius ratios of $\eta = 0.800$ and $\eta = 0.883$. The agreement is within the experimental uncertainties in these cases, and thus supports the assumption of axial periodicity (or infinite cylinder approximation) adopted in this paper.

Table V gives the numerical values of the derivatives appearing in eqs. (2.10) and (3.1), for radius ratios from $\eta = 0.430$ to $\eta = 0.980$, calculated as explained in section 3. Additional computed values not presented, for intermediate radius ratios ($\eta = 0.450, 0.550$, etc.), are consistent with those in this table.

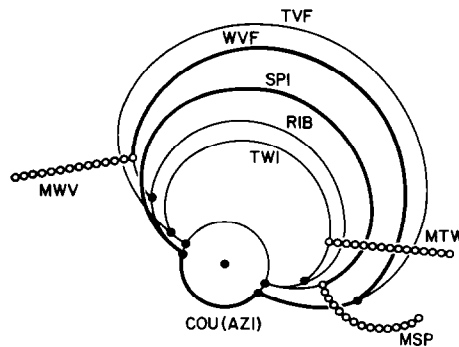


Fig. 6. Gyration bifurcation diagram, with (R_1, R_2) moving in a circular path about the bicritical point as center. Radius ratio $\eta = 0.800$. See the Introduction for explanation of the branch labels. The inner circle represents the trivial Couette flow; radial distance from this circle represents amplitude of the nontrivial flows. Thick lines represent stable branches, thin lines are unstable, and circles represent quasiperiodic solution branches.

All but one of the derivatives in table V are constant in sign, and are monotone functions of η . The single exception is c_ρ^1 , which determines the direction of branching and stability of Taylor vortices; it has a zero near $\eta = 0.87$ and a maximum near $\eta = 0.95$. The coefficient c_ρ^1 was calculated to be negative by Davey [42] and by Kirchgässner and Sorger [43], for $R_2 = 0$ and restricted values of η . Positive values of c_ρ^1 correspond to subcritical Taylor vortices. The sign change found here agrees with the calculations of Jones [21]. The codimension-3 singularity with $c_\rho^1 = 0$ has been considered by Signoret and Iooss [26].

From the data in table V, the bifurcation diagrams are obtained as follows. The direction of branching and stability of all but the quasiperiodic branches of solutions are determined locally by the data in table V, provided only that certain nondegeneracy conditions are satisfied, see Golubitsky and Stewart [4]. If we fix R_2 close to its critical value R_{2c} (but $R_2 \neq R_{2c}$), and vary R_1 as bifurcation parameter, then the bifurcation diagrams are determined by the signs of the following quantities, which must be nonzero for nondegeneracy:

$$\begin{aligned}
 & \text{(a)} \quad c_\rho^1, \\
 & \text{(b)} \quad c_{R_1}^1, \\
 & \text{(c)} \quad (p_\rho^1 + p^3) \cdot c_{R_1}^1 - p_{R_1}^1 \cdot c_\rho^1, \\
 & \text{(d)} \quad (p_\rho^1 - p^3) \cdot c_{R_1}^1 - p_{R_1}^1 \cdot c_\rho^1, \\
 & \text{(e)} \quad p_N^1, \\
 & \text{(f)} \quad p_{R_1}^1, \\
 & \text{(g)} \quad (2 \cdot c_N^1 + c^3) \cdot p_{R_1}^1 - 2 \cdot c_{R_1}^1 \cdot p_N^1, \\
 & \text{(h)} \quad (2 \cdot c_N^1 - c^3) \cdot p_{R_1}^1 - 2 \cdot c_{R_1}^1 \cdot p_N^1, \\
 & \text{(i)} \quad p^2, \\
 & \text{(j)} \quad p_N^1 - p^2, \\
 & \text{(k)} \quad c_N^1 \cdot p_{R_1}^1 + c_{R_1}^1 (p^2 - p_N^1), \\
 & \text{(l)} \quad 2p_N^1 \cdot c_\rho^1 - (p_\rho^1 + p^3) \cdot (2c_N^1 + c^3), \\
 & \text{(m)} \quad 2p_N^1 \cdot c_\rho^1 - (p_\rho^1 - p^3) \cdot (2c_N^1 - c^3), \\
 & \text{(n)} \quad c^3, \\
 & \text{(o)} \quad p^3, \\
 & \text{(p)} \quad c^2, \\
 & \text{(q)} \quad q^3.
 \end{aligned} \tag{4.1}$$

Note that quantities (e), (i), (n), (o), (p) and (q) defined above are already displayed in table V, and all of them are negative for all values of η . Similarly, (b) and (f) are always positive. The remaining quantities in (4.1) are tabulated in table VI. Here we see exactly three sign changes: (a), (j) and (m) each change sign once, between $\eta = 0.87$ and $\eta = 0.95$. These correspond, respectively, to changes of direction of bifurcation (and stability) of Taylor vortex flow (TVF), spirals (SPI) and wavy vortex flow (WVF).

The last entry in table VI is the coefficient for the bifurcation of modulated spirals (MSP) from the spiral flow, calculated as in Crawford et al. [41], see (2.11). It is always positive in the regime $\eta < 0.90$ where spirals are supercritical, which implies that the MSP bifurcation leads to an unstable branch.

All of these data are summarized in the bifurcation diagrams of figs. 5 and 6. In these figures, thick lines represent stable solution branches, thin lines are unstable, and circles represent quasiperiodic branches. The straight branches are those for which the direction and stability has not yet been computed. The labeling of the branches is as defined in Andereck et al. [3] and in the Introduction. In all cases, the branches RIB (ribbons) and TWI (twisted vortices) are unstable.

Fig. 5 shows pairs of conventional bifurcation diagrams, for R_2 constant on either side of its critical value R_2^c , and with R_1 as bifurcation parameter, for $\eta = 0.736, 0.883$ and 0.950 . These bifurcation diagrams are valid locally, for R_2 fixed close to R_2^c , and for R_1 in a small interval containing R_1^c . The pair of bifurcation diagrams shown for $\eta = 0.736$ is typical of all of those obtained in the range $0.43 \leq \eta \leq 0.87$. Note that for $R_2 < R_2^c$, the first bifurcation from Couette flow is always to SPI (spiral flow), and only the SPI branch is stable, in agreement with all previous work on this problem. For $R_2 > R_2^c$, the primary bifurcation from Couette flow is to TVF (Taylor vortex flow), and it is stable as expected. At slightly larger values of R_1 , there is a secondary bifurcation from TVF to stable WVF (wavy vortex flow); this transition had not been reported previously, so close to criticality. The ultimate fate of WVF as R_1 is increased further with R_2 constant cannot be determined from this data. The most interesting feature of fig. 5(a) is the branch of stable SPI not extending to Couette flow, for $R_2 > R_2^c$, where one of TVF or WVF is stable simultaneously. The coexistence of two different stable solutions is called *bistability*; it had not been found before in this context. The SPI branch is initially unstable at the primary bifurcation; it gains stability through a secondary Hopf bifurcation to a torus of quasiperiodic MSP (modulated spirals), calculated as described in Crawford et al. [41] and in section 2. Since the MSP branch bifurcates supercritically and unstably throughout this range, it is not expected to be observable experimentally. However, it can be expected to induce a visible hysteresis jump from SPI to TVF as R_1 is decreased.

As η increases, the region of bistability of SPI and TVF shrinks. Near $\eta = 0.87$, the TVF branch turns subcritical and unstable, see fig. 5(b). Next, the WVF branch turns subcritical as the quantity (4.1)(m) changes sign, and finally, as (4.1)(j) changes sign the SPI branch turns subcritical and unstable near $\eta = 0.92$, see fig. 5(c). It is reasonable to believe that these subcritical branches quickly turn back supercritical and regain stability as the amplitude increases, however direct confirmation of this conjecture would require calculations beyond the scope of the present paper. Thus we cannot rigorously make predictions about the stable (observable) flow patterns for the narrower gaps, $\eta \geq 0.883$, without additional computational effort.

There is still another complication arising in the small gap region. As seen in fig. 4, as $\eta \rightarrow 1$, the bicritical curves for higher modes ($m = 1, 2, 3, \dots$) all come together asymptotically. For example, when $\eta = 0.80$, the value of R_2 for the $m = 1, 2$ bicritical point is about 25% higher than the value for the $m = 0, 1$ bicritical point; at $\eta = 0.883$ this difference is only about 11%. Thus the region of applicability of the analysis in this paper of the $m = 0, 1$ mode interaction shrinks dramatically as $\eta \rightarrow 1$. For the experiments, the proximity of these bicritical curves explains the difficulty encountered by Andereck et al. [3] in resolving flow patterns due to different mode interactions (e.g. IPS), due to the long relaxation times. Therefore, experimentalists investigating mode interaction phenomena are advised to focus their attention on wider gaps which resolve the different mode interactions, e.g. $\eta < 0.85$. At the other end of the scale of η , table IV has shown that the assumption used here to compute the axial wave number k is justified only for $\eta > 0.60$. Thus there is an overlap region, $0.60 < \eta < 0.85$, where both requirements are met, and it is in this region that agreement of this paper with experiments may be sought.

Fig. 6 displays the same type of information as fig. 5, but in the form of a *gyrant bifurcation diagram*, that is, a diagram which plots the amplitude of a solution branch radially from a unit circle, as a function of the angles as (R_1, R_2) moves around a circle centered at the bicritical point in the (R_1, R_2) plane. Recent advances in computer-controlled instrumentation allow the experimentalist to program the ap-

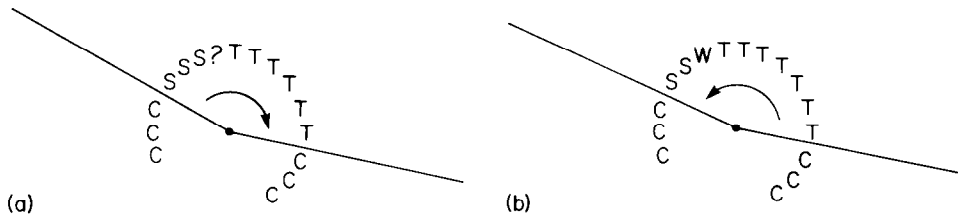


Fig. 7. Experimentally observed states near the bicritical point, for $\eta = 0.800$. In the experiments, R_1 and R_2 were varied in steps on a circular path around the bicritical point (stepsize about one unit in Reynolds number). The letters indicate the observed state, e.g. C is Couette flow. (a) Clockwise circuit showing transition from spirals (S) directly to Taylor vortices (T). (b) Counterclockwise circuit, showing transitions from Taylor vortices to wavy Taylor vortices (W) then to spirals.

paratus to follow this type of path in the (R_1, R_2) plane, see fig. 7. Gyrant bifurcation diagrams as in fig. 6 have several advantages over the traditional bifurcation diagrams in fig. 5. They are uniformly valid for parameter values (R_2, R_1) in a sufficiently small disk centered at the bicritical point, and thus they eliminate the singularities due “north and south” of the bicritical points, showing how the branches on the left and right of bicriticality are connected.

Fig. 6 with $\eta = 0.800$ makes clear the bistability and hysteresis behavior. It shows that the isolated stable SPI branch shown in fig. 5 for $R_2 > R_2^c$ is in fact joined to the stable SPI branch for $R_2 < R_2^c$. Moreover, it shows that the WVF branch continues over the “north pole” and is stable in a region to the left of bicriticality. It clearly predicts the existence of a *hysteresis loop*, with transitions occurring between SPI and TVF or WVF, in both directions but at different angles, as (R_1, R_2) traverses the circular path. The bifurcations of MWV (modulated wavy vortices) and MTW (modulated twisted vortices) are indicated by straight branches (of small circles), because the direction and stability of these branches has not yet been computed; however WSP has been computed and is unstable, as noted above.

Fig. 7 presents some preliminary results from experimental studies of Tagg et al. [5], around the bicritical point for $\eta = 0.800$, motivated by the theoretical work in this paper. These experiments have revealed the existence of WVF, bistability, and hysteretic transitions depending on the direction of the path around the bicritical point. Fig. 7 shows all of the stable flow patterns predicted theoretically in fig. 6, and they occur in the same order, around the bicritical point in either direction. This agreement is remarkable in view of the experimental difficulties caused by the long transient times near the bicritical point, and the local validity of the calculations, as well as the idealized assumptions of periodic boundary conditions and equal axial wave numbers. The weaker quantitative agreement between figs. 6 and 7 in the numerical values of these transitions may be due to these idealizations.

Very recent experiments of Tagg and Swinney [44] have revealed a new “alternating spirals” flow, occurring after spirals lose stability and before Taylor vortices gain stability during the clockwise circuit of the codimension-two point. This new mode is indicated by a question mark in fig. 7. Here one observes simultaneous upward and downward spirals in opposite ends of the cylinder, separated by an interface which slowly oscillates axially, with a period up to 70 times that of the basic spirals period. This may be a type of stable homoclinic behavior, or may correspond to quasiperiodic flow on a torus, but it is not yet explained by theory.

In conclusion, this work has yielded new understanding of the process of pattern formation in the Taylor–Couette experiment, and already has led to new experimental findings. These successes suggest that the same methods of equivariant bifurcation theory can be fruitfully applied to investigations of pattern formation in other contexts.

Acknowledgements

The authors thank R. Tagg and H.L. Swinney for their help in relating this work to the experiments, and for allowing us the use of the photographs in fig. 2. We also thank J.D. Crawford, W.W. Farr and W. Nagata for help with the calculations reported in table III. This research was supported at the University of Houston by the ACMP program of DARPA, by NASA Ames Grant 2-279, and by the Energy Laboratory of the University of Houston, and at the University of Guelph by NSERC, Canada. One of us (WFL) thanks the University of Houston for visiting positions in 1985 and 1987.

References

- [1] G.I. Taylor, Stability of a viscous liquid contained between two rotating cylinders, *Phil. Trans. Roy. Soc. London A* 223 (1923) 289–343.
- [2] R.C. DiPrima and H.L. Swinney, Instabilities and transition in flow between concentric rotating cylinders, in: *Hydrodynamic Instabilities and the Transition to Turbulence*, H.L. Swinney and J.P. Gollub, eds., *Topics in Applied Physics* 45 (Springer, Berlin, 1981), pp. 139–180.
- [3] C.D. Andereck, S.S. Liu and H.L. Swinney, Flow regimes in a circular Couette system with independently rotating cylinders, *J. Fluid Mech.* 164 (1986) 155–183.
- [4] M. Golubitsky and I. Stewart, Symmetry and stability in Taylor–Couette flow, *SIAM J. Math. Anal.* 17 (1986) 249–288.
- [5] R. Tagg, B. Dornblaser, W.S. Edwards and H.L. Swinney, Critical dynamics near the spiral–Taylor vortex codimension-two point, in preparation (1988).
- [6] G. Ahlers, D.S. Cannell, M.A. Dominguez-Lerma and R. Heinrichs, Wavenumber selection and Eckhaus instability in Couette–Taylor flow, *Physica D* 23 (1986) 202–219.
- [7] H.A. Snyder, Stability of rotating Couette flow, I. Asymmetric waveforms; II. Comparison with numerical results, *Phys. Fluids* 11 (1968) 728–734 and 1599–1605.
- [8] E.R. Krueger, A. Gross and R.C. DiPrima, On the relative importance of Taylor-vortex and nonaxisymmetric modes in flow between rotating cylinders, *J. Fluid Mech.* 24 (1966) 521–538.
- [9] T.B. Benjamin, Bifurcation phenomena in steady flows of a viscous fluid II. Experiments, *Proc. Roy. Soc. London A* 359 (1978) 27–43.
- [10] M. Golubitsky, I. Stewart and D. Schaeffer, *Singularities and Groups in Bifurcation Theory*, vol. 2, *Appl. Math. Sci.* 69 (Springer, New York, 1988).
- [11] P. Chossat, Y. Demay and G. Iooss, Interaction de modes azimutaux dans le probleme de Couette–Taylor, *Arch. Rat. Mech. Anal.* 99 (1987) 213–248.
- [12] W.F. Langford, Periodic and steady-state mode interactions lead to tori, *SIAM J. Appl. Math.* 37 (1979) 22–48.
- [13] P. Holmes, Unfolding a degenerate nonlinear oscillator: a codimension two bifurcation, *Ann. N.Y. Acad. Sci.* 357 (1980), *Nonlinear Dynamics*, R.H.G. Helleman, ed., pp. 473–488.
- [14] G. Iooss and W.F. Langford, Conjectures on the routes to turbulence via bifurcations, *Ann. N.Y. Acad. Sci.* 357 (1980), *Nonlinear Dynamics*, R.H.G. Helleman, ed., pp. 489–505.
- [15] J. Guckenheimer, On a codimension two bifurcation, in: *Dynamical Systems and Turbulence*, Warwick 1980 Proc., D.A. Rand and L.-S. Young, eds., *Lecture Notes in Math.* (Springer, Berlin, 1981), pp. 99–142.
- [16] J. Guckenheimer and P. Holmes, *Nonlinear Oscillations, Dynamical Systems, and Bifurcation of Vector Fields*, *Appl. Math. Sci.* 42 (Springer, New York, 1983).
- [17] W.F. Langford, R. Tagg, E. Kostelich, H.L. Swinney and M. Golubitsky, Primary instabilities and bicriticality in flow between counterrotating cylinders, *Phys. Fluids* 31 (1988) 776–785.
- [18] A. Davey, R.C. DiPrima and J.T. Stewart, On the instability of Taylor vortices, *J. Fluid Mech.* 31 (1968) 17–52.
- [19] P.M. Eagles, On the stability of Taylor vortices by fifth order amplitude expansions, *J. Fluid Mech.* 49 (1971) 529–550.
- [20] R.C. DiPrima and R.N. Grannick, A nonlinear investigation of the stability of flow between counter-rotating cylinders, in: *Instability of Continuous Systems*, H. Leipholz, ed. (Springer, Berlin, 1971), pp. 55–60.
- [21] C.A. Jones, On flow between counter-rotating cylinders, *J. Fluid Mech.* 120 (1982) 433–450.
- [22] P. Chossat and G. Iooss, Primary and secondary bifurcations in the Couette–Taylor problem, *Jap. J. Appl. Math.* 2 (1985) 37–68.
- [23] Y. Demay and G. Iooss, Calcul des solutions bifurquées pour le problème de Couette–Taylor avec les deux cylindres en rotation, *J. Meca. Th. Appl.*, Vol. Spécial, “Bifurcations et comportements chaotiques” (1985) 193–216.

- [24] P. Chossat and M. Golubitsky, Hopf bifurcation in the presence of symmetry, center manifold and Liapunov–Schmidt reduction, in: *Oscillation, Bifurcation and Chaos*, F.V. Atkinson, W.F. Langford and A.B. Mingarelli, eds., CMS Conf. Proc. 8 (1987) 343–352.
- [25] P. Laure and Y. Demay, Symbolic computation and equations on the center manifold: application to the Taylor–Couette problem, *Computers and Fluids* (1986), to appear.
- [26] F. Signoret and G. Iooss, Une singularité de codimension 3 dans le problème de Couette–Taylor, *Prep. Math. No. 142* (1987), Université de Nice, France.
- [27] P. Laure, Bifurcation secondaire de solutions quasi-périodiques pour le problème de Couette–Taylor, *C.R. Acad. Sci. Paris Sér. I* (1987) 305 493–496.
- [28] R.C. DiPrima, P.M. Eagles and J. Sijbrand, Bifurcation near multiple eigenvalues for the flow between concentric counterrotating cylinders, in: *Numerical Methods for Bifurcation Problems*, T. Küpper, H.D. Mittelman and H. Weber, eds., ISNM 70 (Birkhäuser, Boston, 1984), pp. 495–501.
- [29] O.E. Lanford III, The strange attractor theory of turbulence, *Ann. Rev. Fluid Mech.* 14 (1982) 347–364.
- [30] J. Guckenheimer, Strange attractors in fluids: another view, *Ann. Rev. Fluid Mech.* 18 (1986) 15–31.
- [31] A. Brandstätter, J. Swift, H.L. Swinney and A. Wolf, A strange attractor in a Taylor–Couette experiment, in: *Turbulence and Chaotic Phenomena in Fluids*, T. Tatsumi, ed., IUTAM (North-Holland, Amsterdam, 1984), pp. 179–184.
- [32] W.F. Langford, Chaotic dynamics in the unfoldings of degenerate bifurcations, *Proc. Int. Symp. on Appl. Math. and Computer Sci.*, Kyoto University, Japan (1982), pp. 41–47.
- [33] W.F. Langford, Numerical studies of torus bifurcations, in: *Numerical Methods for Bifurcation Problems*, T. Küpper, H.D. Mittelman and H. Weber, eds., ISNM 70 (Birkhäuser, Boston, 1984), pp. 285–295.
- [34] D.H. Sattinger, *Topics in Stability and Bifurcation Theory*, Lect. Notes in Math. 309 (Springer, New York, 1973).
- [35] S. Chandrasekhar, *Hydrodynamic and Hydromagnetic Stability* (Oxford University Press, Oxford, 1961).
- [36] R. Temam, *Navier–Stokes Equations and Nonlinear Functional Analysis*, CBMS-NSF Reg. Conf. Ser. in Appl. Math. 41 (SIAM, Philadelphia, 1983).
- [37] G. Iooss, Bifurcation and transition to turbulence in hydrodynamics, CIME session on Bifurcation Theory and Applications, L. Salvadori, ed., *Lect. Notes in Math.* 1057 (Springer, Berlin, 1984), pp. 152–201.
- [38] W.F. Langford, Equivariant normal forms for the Taylor–Couette problem, in: *Multiparameter Bifurcation Problems*, M. Golubitsky and J.M. Guckenheimer, eds., *Contemp. Math.* 56 (1986) 363–365.
- [39] M. Golubitsky and I. Stewart, Hopf bifurcation in the presence of symmetry, *Arch. Rat. Mech. Anal.* 87 (1985) 107–165.
- [40] C. Elphick, E. Tirapegui, M.E. Brachet, P. Coulet and G. Iooss, A simple global characterization for normal forms of singular vector fields, *Physica D* 29 (1987) 95–127.
- [41] J.D. Crawford, M. Golubitsky and W.F. Langford, Modulated rotating waves in $O(2)$ mode interactions, *Dyn. Stab. Syst.* (1988), to appear.
- [42] A. Davey, The growth of Taylor vortices in flow between rotating cylinders, *J. Fluid Mech.* 14 (1962) 336–368.
- [43] K. Kirchgässner and P. Sorger, Branching analysis for the Taylor problem, *Quart. J. Mech. Appl. Math.* 22 (1969) 183–209.
- [44] R. Tagg and H.L. Swinney, Spontaneous alternation of travelling waves in spiral vortex flow between counterrotating cylinders, in preparation (1988).
- [45] M. Golubitsky and D. Schaeffer, *Singularities and Groups in Bifurcation Theory*, vol. 1, *Appl. Math. Sci.* 51 (Springer, New York, 1985).
- [46] P. Chossat and M. Golubitsky, Iterates of maps with symmetry, *SIAM J. Math. Anal.* 19, No. 6 (1988), to appear.